Table of Contents for Chapter 4

Chapter 4

Research Goals and Plans for Boundary Physics

4.1. Overview of goals and plans

Control of the plasma-material interface is a key research area [1, 2, 3] for present and future tokamaks. There are a number of research gaps and required actions needed for ST-FNSF design activities. Indeed recent research in this area has raised concerns about ITER heat exhaust scenarios as well [4, 5, 6].

The NSTX-U will provide a significant advance over the existing STs capabilities to enable world-class, and in certain areas, world-leading boundary physics research. Doubling the I_p and B_t will enable higher confinement, stored energy and H-mode pedestal density and temperature, but will likely also further concentrate heat and particles fluxes on the plasma facing components (PFCs). The increase in the input power is needed to achieve
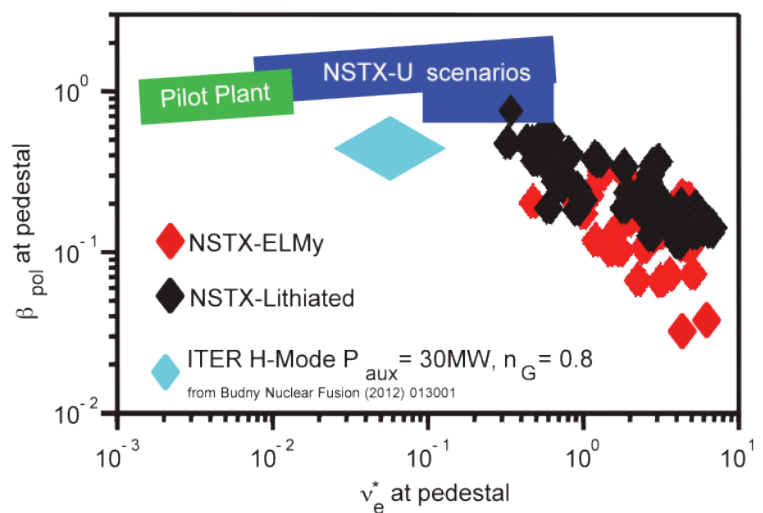
Figure 4.1.1: Pedestal poloidal beta and collisionality expected to be accessible in NSTX-U.

4.2
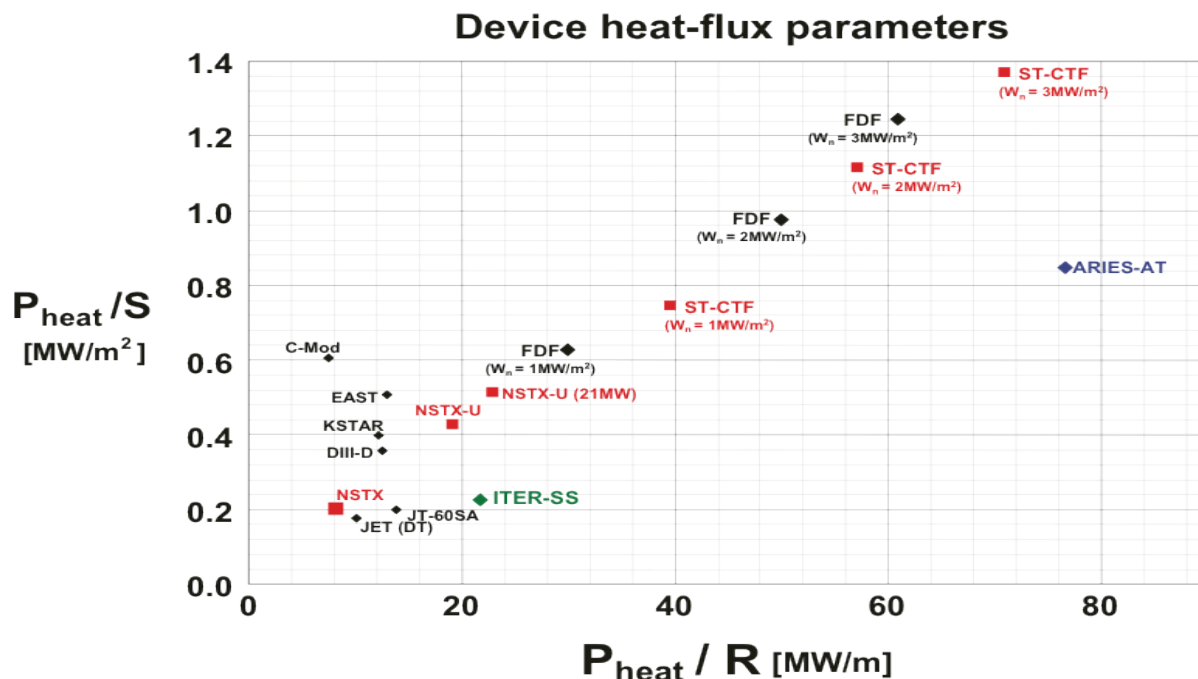
Figure 4.1.2: *Heating power normalized to plasma surface area (P/S) and major radius (P/R) for present and proposed tokamaks.*

low ν^* at higher I_p and B_t. Figure 4.1.1 shows the expected range in pedestal ν^* and pedestal β_{pol} in NSTX, and the projected range for NSTX-U, ITER, and a Pilot Plant.

Coupled with the ~ 5x extension of pulse length, the augmented heating power will increase the magnitude of the required energy removal from the PFCs between discharges. Two measures of divertor loading are given by P_{heat}/R and P_{heat}/S, where R and S are the major radius and surface area of the device respectively. Figure 4.1.2 shows that capability projected for NSTX-U in these parameters will meet or exceed the capabilities of existing fusion facilities.

In developing an integrated solution that insures successful power and particle control compatible with an attractive core plasma, a mix of innovative and proven conventional technologies will be deployed.

With these considerations in mind, the Boundary Physics goals over the next five years on NSTX-U include several main aspects:
- Support the central mission of NSTX-U, i.e., reduced ν^* fully non-inductive high-β steady-state core H-mode operation development, enabled in part by active particle control via cryo-pumping and lithium PFCs; this bullet encapsulates contributions of boundary physics to the first two overall NSTX-U goals in Chapter 1
- Exploit unique ST and NSTX-U features, e.g., low edge ν^*, high plasma current, high divertor heat flux and compact design, to improve physics understanding of edge heat and

4.3

particle transport for validation of novel snowflake and conventional radiative solutions of the plasma-material interface; this bullet connects to the overall NSTX-U goal #4 from Chapter 1

- Control and optimize the H-mode pedestal and edge localized modes (ELMs), as the pedestal represents the key interface between the core physics and divertor physics goals described in the two bullets above; this is necessary to achieve the two goals above with an integrated core-edge solution
- Evaluate the impact of high-Z PFCs on the edge and core plasma, as they are deployed in NSTX-U; this bullet connects to the overall NSTX-U goal #5 from Chapter 1

Below, the three dedicated Thrusts in this part of the program are mapped to these areas, with detailed descriptions given in the next section.

4.1.1 Thrust BP1: Characterize, control, and optimize the H-mode pedestal performance, transport, and stability

Background: H-mode Pedestal and ELM control includes characterization of the L-H transition, pedestal structure, turbulence, and edge stability in ELMy and ELM-free discharges, extending studies done in NSTX to lower ν^*, while making use of new capabilities in NSTX-U. The lower ν^* is expected to affect the pedestal in many ways, e.g. 1) the bootstrap current will be increased; 2) the intermediate collisionality enhancement [144] of bootstrap current relative to the Sauter formulation [145] will decrease; 2) possible re-ordering of which micro-instabilities (micro-tearing vs. hybrid Trapped Electron Mode (TEM)/Kinetic Kallooning Mode (KBM) vs. Electron Temperature Gradient (ETG)) dominate pedestal transport; 3) possible re-ordering of the importance of 2-D particle transport vs. 3-D expected particle transport with application of magnetic perturbations, which could lead to density pump-out in NSTX-U, which was never observed in NSTX H-mode discharges. This thrust also entails pedestal control via the use of ELM pace-making via either pulsed 3-D fields or injected granules or pellets, as well as access to advanced/alternate edge stability regimes, such as the Enhanced Pedestal H-mode and I-mode.

Thrust text: NSTX-U researchers will characterize the L-H mode transition thresholds utilizing the extended field, current, and power range of NSTX-U and by measuring turbulence and zonal flow dynamics with beam emission spectroscopy, Doppler backscattering, and gas-puff imaging diagnostics. The maximum achievable pedestal height and variation in pedestal structure will be assessed as a function of increased field, current, and power and also shaping and measured with enhanced spatial and temporal resolution Thomson Scattering. Increased control of pedestal transport and stability will be attempted using such techniques as edge density profile modification with improved fueling control, extended lithium coating coverage, and cryo-pumping. ELM triggering and suppression with 3D fields from mid-plane (existing) and off-midplane NCC coil-sets and also triggering with lithium granule injection will be assessed.

Enhanced pedestal H-modes (EP H-modes) will be further explored. As high-Z PFCs are introduced, their compatibility with good H-mode pedestal performance will be assessed.

4.1.2 Thrust BP-2: Control divertor heat fluxes with a combination of innovative and proven techniques

Background: Heat flux scaling experiments in NSTX and other devices have identified a strong inverse dependence of the extrapolated midplane heat flux width, λ_q^{mid}, on plasma current [57], with no dependence on B_t or input power. Fortunately the divertor heat flux footprint width was shown to increase with flux expansion [129]. Projections for NSTX-U based on NSTX data indicate a peak heat as high as 40-50 MW/m^2, in low flux expansion, high heating power scenarios (see Chapter 9). Thus heat flux handling will be crucial not only for projection to future devices, but also for achievement of full I_p, full B_t, long pulse NSTX-U plasmas. Validation of novel and conventional solutions for heat exhaust at the high P/R and P/S in NSTX-U includes both high flux expansion 'snowflake' divertor configurations, as well as radiative divertor configurations. Along with the TCV device [81, 82, 83], NSTX pioneered the use of the 'snowflake' configuration, demonstrating control of the heat flux and a strong effect on ELM stability [84]. In addition, radiative divertor operation was successfully demonstrated in highly shaped, high performance NSTX discharges [73], extending a technique demonstrated in higher aspect ratio tokamaks [130]. As shown in Chapter 9, successful high flux expansion configurations and/or radiative dissipation is projected to reduce peak heat flux to acceptable values.

Thrust text: NSTX-U research efforts will investigate the SOL heat and particle transport and turbulence and associated flux-widths extending the existing NSTX database to lower $\nu*$, higher I_P, and P_{SOL}. Measurements will be compared to multi-fluid turbulence and gyro-kinetic models. Novel divertor geometries such as the snowflake divertor will be systematically investigated for power and particle control and magnetic control of divertor configurations will be developed to support standard and snowflake divertor configuration studies. Steady-state and transient heat and particle transport and divertor PFC loads in these configurations will be studied as a function of magnetic balance, magnetic configuration parameters, feedback-controlled impurity seeding rate over a range of SOL powers and widths. Highly-radiating boundary solutions with feedback control will be developed, and divertor detachment operating window and access parameters will be studied. As high-Z PFCs are introduced, their compatibility with the divertor heat exhaust solutions will be assessed.

4.1.3 Thrust BP-3: Compare the sustainability of particle exhaust via lithium pumping and cryo-pumping, for density, impurity, and Z_{eff} control consistent with integrated scenarios

Background: Integrated scenarios on NSTX-U are designed for steady density at 0.5-1 times Greenwald density limit scaling [146]. To achieve this, a central element of the boundary program is installation of a divertor cryo-pump, representing a proven technology to control both main ion and impurity density. A key component of the research is to compare lithium pumping and cryo-pumping for density control, while considering the possible synergy of the two techniques to contribute to the required power and particle exhaust solution for future devices and NSTX-U itself. An integral element to both of these studies is the assessment of impurity sources and transport.

Thrust text: Experiments will be conducted to validate cryo-pump physics design activities, perform initial density control studies, and assess compatibility with H-mode pedestal and core performance and divertor power exhaust scenarios. Comparisons will be made between lithium conditioning and cryo-pumping for density and impurity control, as well as changes to the edge density profile, which are central to ELM elimination with lithium conditioning. Local recycling coefficients in the upper and lower divertor regions, as well as the wall will be measured. Impurity sources and SOL transport, and the role of ELMs in impurity control will be assessed. As high-Z PFCs are introduced to NSTX-U, their impact on core impurity transport, boron and lithium coatings, and divertor retention and particle control will be assessed.

As evident from the texts of the thrusts, the use of lithium touches nearly all areas of boundary physics, and as such represents a valuable tool. From a particle control standpoint, lithium has been shown to control plasma deuterium content; the sustainability of this effect [103], along with its dependence on the increased NSTX-U capabilities, needs to be determined. In addition, the reduced recycling from lithium conditioning has been shown to modify the edge density/pressure profiles and ELM stability, improving H-mode pedestal performance [7, 8, 9]. Finally, lithium affects both the peak heat flux profile and magnitude. At low to intermediate pre-discharge evaporation, the footprint narrows and the peak heat flux increases; at high evaporation rates, the peak heat flux itself is reduced, possibly from evaporative cooling [131]. The detailed studies in NSTX-U, derived from NSTX observations, are laid out primarily in the Materials and PFCs chapter, but specific contributions to the boundary program are described in the individual sections below.

4.2. Research Areas

4.2.1. Thrust BP-1: Characterize, control, and optimize the H-mode pedestal performance, transport, and stability

H-mode access is important for NSTX-U to accomplish its high-performance, non-inductive, long-pulse mission, and it is also a critical issue for future advanced tokamaks, such as ITER.

The H-mode is characterized by a factor-of-two improvement in global energy confinement due to the reduction of radial heat and particle transport across the plasma, but especially in a narrow region near the plasma boundary, referred to as the H-mode pedestal. This allows for a broad core pressure profile leading to improved core plasma magneto-hydrodynamic (MHD) stability, albeit with a large edge pressure gradient and associated bootstrap current that can destabilize edge-localized instabilities termed "ELMs". Access to the H-mode regime requires sufficient plasma heating power such that the power lost through the plasma boundary exceeds a threshold (P_{LH}). The new capabilities of NSTX-U, including an expanded operating range, lower ν^*, expanded spectrum of applied 3D fields, a second neutral beam that will allow for modifying the rotation and current profiles, and a variety of wall conditioning and particle control techniques, will be utilized to study P_{LH}, and improve understanding and control of the H-mode pedestal.

In the following sections, L-H transition research and the ensuing ELM/pedestal dynamics will be described, followed by a discussion of the pedestal transport and stability research and plans. This will be followed by a discussion of tools that have been and will be used to control ELMs through control of the pedestal structure.

4.2.1.1   L-H Transition Physics

a. Power threshold studies
The L-H transition and the subsequent pedestal formation is a multi-scale process, meaning that the important physics spans many orders of magnitude in space and time. Advances in plasma diagnostics and computational resources will allow NSTX-U researchers to examine spatial and temporal phenomena on spatial scales of several cm down to fractions of an ion gyroradius, and on temporal scales from <kHz up to 100 kHz, covering the ranges expected to be important for the L-H transition physics. NSTX-U can contribute to the development of first principles models for the L-H transition in several critical ways, including (1) investigating the impact of X-point geometry (X-point position, up/down magnetic balance, grad-B drift direction) in unique divertor configurations and with independent X-point control at both the top and bottom of the device; (2) decoupling the X-point geometry and divertor recycling effects by leveraging lithium deposition, which is capable of pumping a wide variety of strike point locations, and with the mid-term installation of the lower divertor cryo-pump; (3) studying the impact of 3D fields taking advantage of an expanded spectrum of applied perturbations, with the installation of in-vessel coils in the middle of the Five Year plan; (4) comparing RF and NBI heating; and (5) exploring the effects of aspect ratio by comparing to higher R/a devices, by measuring and assessing the importance of zonal flows, Geodesic Acoustic Modes (GAMs), and turbulence in initiating and sustaining the H-mode. Furthermore, NSTX-U will be able to perform these studies in an expanded operating regime and with more control of density, and rotation and current profiles.

The present L-H power threshold scaling from the ITPA multi-machine database is given by: $P_{LH} = 0.0488 \, n_{el}^{0.717} \, B_t^{0.803} \, S^{0.941}$ where the units are P_{LH} [MW], line average electron density n_{el} in 10^{20} m^{-3}, B_t in T, and surface area S in m^2 [132]. Relative to this scaling, both large low R/a devices NSTX and MAST also measured an increasing P_{LH} with I_p [133]. Access to higher I_p and the new measurement capabilities will facilitate unfolding of the underlying physics, which is needed for projection to a low R/a FNSF which will operate at substantially higher I_p than today's devices.

Other dependences to P_{LH} beyond the standard scaling are typically referred to as "hidden parameters"; this is another area in which NSTX made contributions. It was observed on NSTX that P_{LH} decreased as the triangularity decreased (larger X-point radius), as the I_p decreased, as the amount of pre-discharge lithium increased, and the fraction of inboard / outboard neutral fueling increased [10, 11, 12]. Dedicated experiments and subsequent modeling using the full-f kinetic neoclassical XGC0 code[13] indicated that the P_{LH} scaling with R_X and I_p was due, in part, to changes in the edge E × B shear driven by an ion orbit loss hole. The dependence of P_{LH} on the poloidal location of the neutral fueling (inboard, outboard or divertor) was also shown to impact the neutral penetration and fueling efficiency. As the fueling efficiency decreased, the neutral density at the separatrix increased which could lead to more energy loss to charge-exchange and ionization and thus enhanced edge E × B shear that could initiate and sustain the H-mode. Experiments on NSTX also studied the scaling of P_{LH} versus a variety of other plasma parameters, such as toroidal field, electron density, ion species, n=3 field amplitude, X-point balance, grad-B drift direction, wall conditioning and heating balance (ohmic, NBI and RF). These experiments also documented the edge conditions (T, n, v, and their gradients) at the time of the transition.

Because of limitations in control and conditioning capabilities in NSTX, isolating the various effects of geometry and wall conditioning (or recycling) was difficult. The broader range of NSTX-U capabilities to be implemented over the five-year period, however, will enable dedicated studies in which these effects can be isolated. Recycling control will be studied in experiments comparing boronization and lithiumization for wall conditioning, using both downward and upward facing lithium evaporators for increased coverage of the PFCs and for strong pumping on all the divertor legs, and the eventual implementation, in the middle of the Five Year research period, of a cryo-pump situated in the lower divertor.

Application of n=3 3-D fields in NSTX was found to lead to a ~50% increase in P_{LH}. The reason for this is still under study, with e.g. neoclassical and turbulence calculations. It was the case, however, that the limited power supplies in NSTX allowed for only one non-resonant component of the field to be applied for these studies. NSTX-U plans to have six independently controlled radial field coils (NCC) at the outboard midplane, and this will allow for more flexibility in the

mode spectrum of the applied perturbations. Furthermore, midway into the five year research period, a partial set of in-vessel, off-midplane coils will be installed, enabling even more poloidal harmonic flexibility. The coil system will thus provide the tools to study the impact of resonant and non-resonant magnetic field perturbations on the L-mode transport leading up to L-H transition, the L-H transition itself, and the subsequent pedestal growth. Of particular interest is the interaction of flows and turbulence with non-axisymmetric magnetic fields. Another feature of the upgraded and new 3D coil systems is that they will give the capability, in various coil combinations, to vary the edge Neoclassical Toroidal Viscosity (NTV) to enable isolation of 3D effects from rotation effects. Varying the NTV effectively allows for rotation control for a given combination of neutral beam sources. Additional torque variations to control the rotation in the core and mid-plasma region can be provided by a combination of sources from both the original and the new, more tangentially-directed, neutral beams.

b. Turbulence changes

The formation of the edge transport barrier and its correlation with turbulence suppression were investigated in NSTX using a variety of diagnostics, including the ultrafast-swept FMCW reflectometers, gas-puff imaging (GPI) and beam emission spectroscopy (BES). The k_r spectra and radial correlation lengths across the edge region indicate that turbulence across the entire k_r spectrum is suppressed and the correlation length decreases at the time of the transition. This is coupled to an increase in the local electron density gradient, demonstrating a clear correlation between the transport barrier formation and turbulence suppression. This low-k turbulence re-appears during the natural density ramp that precedes the first naturally ELM, and between subsequent ELMs. Oscillatory behavior of the poloidal flow is often observed prior to the transition and resembles limit-cycle oscillations of zonal flows/GAMs near the separatrix, as measured by the GPI diagnostic[14, 15]. These flows were correlated with quiet periods in the edge turbulence preceding the L-H transition[14]; similar oscillations have been seen on ASDEX-Upgrade, TJ-II, DIII-D, EAST, and HL-2A [147] suggesting a common phenomenon. In some cases, however, these zonal flow spectra are broadband and intermittent, rather than coherent with a frequency ~3 kHz.

The enhanced capability of NSTX-U, especially with a broader range of turbulence diagnostics and techniques to vary the ExB shear, will allow a more comprehensive investigation of the turbulence dynamics and evolution from the L-phase into the H-phase. These turbulence diagnostics will measure density fluctuations across the range from ion gyroradius (BES) to electron gyroradius (microwave scattering) scales, and, in addition, a polarimetry diagnostic will be able to measure magnetic field fluctuations in the long wavelength (ion gyroradius scale) regime. The similarities and differences in the L-H transition dependences, dynamics and associated turbulence changes between NSTX-U and higher aspect ratio devices will provide the leverage necessary to test and validate the leading theories of the L-H transition.

4.2.1.2 Pedestal Structure and Edge Localized Mode Physics

The H-mode pedestal formation and evolution following the L-H transition is critical in optimizing fusion performance, both for NSTX-U and future next-step devices such as FNSF. It follows that being able to predict the pedestal structure (heights, widths, gradients) is crucial for determining the parameters in the design of future devices.

Control of the edge pedestal will be necessary in future devices such as ITER, since the observed natural tendency of most H-modes is toward a state with ELMs, that result in periodic edge plasma ejection, and unacceptable PFC erosion when extrapolated to future devices. Since the pedestal performance is strongly correlated with global plasma confinement [148], pedestal control must be done in a way that preserves high pedestal pressures without large ELMs. Furthermore, the edge particle transport must be made sufficiently large that density and impurity levels in the core plasma are controlled—something that does not occur in traditional ELM-free H-modes, which usually suffer from impurity accumulation. An introduction to ELM physics is given here, along with outstanding questions for investigation in NSTX-U.

4.2.1.2.1 Physics of ELMs

ELMs are periodic ejections from the edge plasma[149], thought to be triggered when the edge pressure gradient and/or current density exceed ideal or resistive MHD limits[34]. Violation of the stability criteria leads to the onset of Peeling Ballooning Modes (PBM), in which the instability drive comes from both the pressure gradient and current density [22; 150]. There are often coherent oscillations in magnetic probe signals that precede the ELM crash; these represent the growth of the mode itself. The issues related to ELM research include:
- Identifying common characteristics in the phenomenology of different ELM Types
- Physics of the underlying instabilities
- Transport of ELM heat and particle flux in the SOL, and incident at the divertor and wall

A wide variety of ELMs, driven by different instabilities, have been identified on fusion devices [151; 152]. In NSTX, large Type I ELMs, intermediate Type III ELMs at low and high collisionality, and tiny Type V ELMs appearing in a wide operating space have been observed [31]. The discussion below focuses on the two most common ELM types in NSTX: large Type I and small Type V. Type II ELMs have also been identified, but only in a narrow operating window in edge β and magnetic balance very near double-null configuration [32].

The correlation between violation of PBM stability, which limits the total pedestal height and width, and Type I ELM onset has been established in a large number of devices [25], including

NSTX. Substantial edge stability analysis was done for Type I ELMy discharges in NSTX, particularly in scans with increasing lithium conditioning in which ELMs gradually disappeared[7, 9]. It was generally found that these ELMs correspond to violation of the PBM stability limits, e.g. as shown in Figure 4.2.1. In general, NSTX plasmas tended to be driven more by current driven modes than pressure driven modes [7, 9, 23] owing to the strong stabilization of high-n ballooning modes at low R/a [26]. Only with 'weak' shaping of the plasma, i.e. at low triangularity and elongation, did the ballooning boundary re-appear in stability diagrams [27].
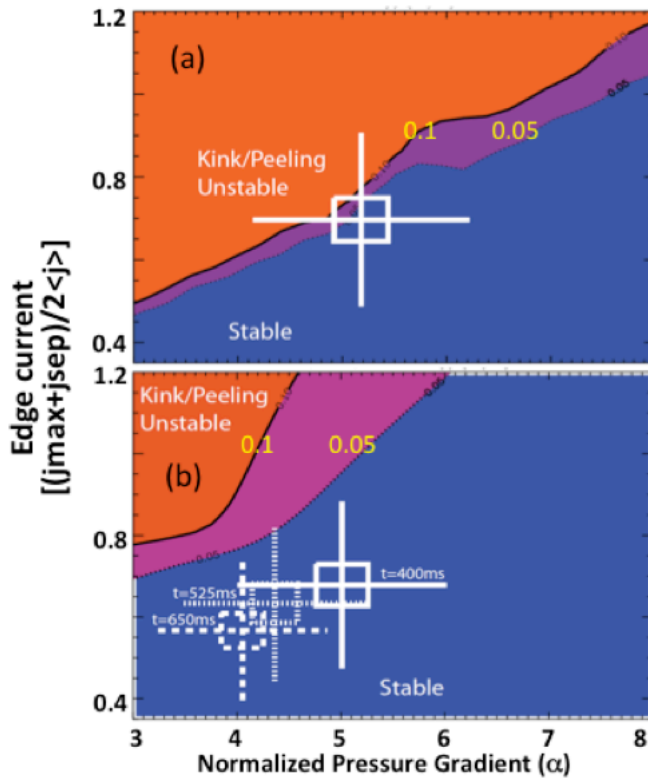

Figure 4.2.1: Comparison of edge stability for (a) Type I ELMy H-mode and (b) lithiated ELM-free H-mode (three time-slices). Contours of the linear growth rate normalized to the diamagnetic drift frequency are plotted, with the purple contour representing the instability transition (given by orange color). The experimental data point and error bars are represented by the white crosses [7].

The use of lithium wall conditioning drastically improved the Type I ELM stability in NSTX, e.g. Figure 4.2.1b [7, 8, 9]. First, a nearly continuous improvement of a number of discharge characteristics, e.g. reduced recycling, ELM frequency, and edge electron transport, with increasing pre-discharge lithium evaporation on graphite PFCs was observed. Profile and stability analysis clarified the mechanism responsible for ELM avoidance and the role of lithium. Lithium coatings reduced recycling and core fueling; thus the density and its gradient near the separatrix were reduced. The T_e gradient near the separatrix was unaffected, possibly due to the exacerbation of ETG modes; hence the pressure gradient and bootstrap current near the separatrix were reduced, leading to stabilization of the PBM thought to be responsible for the NSTX ELMs. It is worth noting that the change of the edge gradients with lithium conditioning was qualitatively reproduced with the paleoclassical transport model [8]. Thus, the enhanced edge stability with lithium coatings was correlated with the reduction of the pressure and its gradient near the separatrix. The key ingredient for ELM avoidance was control of the particle channel *independent* of the thermal channel at the edge: the density profile was continuously manipulated

via the amount of lithium evaporation and resulting recycling control, leading to reduced neutral fueling and relaxed n_e observed gradients.

Figure 4.2.1 also highlights an outstanding question: the linear growth rate of the instability was typically ~ 5-10% of the diamagnetic drift frequency. Normally medium and high-n instabilities with growth rates up to 50% of the drift frequency are computed to be stabilized by the diamagnetic drift. Recently XGC0 was used to directly compute the bootstrap current, to compare with the Sauter formulation. It was found that at intermediate ν^* and low R/a typical of ELMy H-modes in NSTX, the XGC0 bootstrap current was 30-50% higher than Sauter [153], leading to higher ideal growth rates than originally computed[7].

At present, the Type V ELMs appear to have been unique to NSTX operation [33]. These were single or double filament instabilities that propagated in the electron drift direction, and were correlated with operation with boronized walls. With sufficient pre-discharge lithium that raised edge temperatures, Type V ELMs were suppressed, pointing to resistive instabilities. The appeal of this research is easily stated: these ELMs could provide sufficient particle and impurity control with minimal heat flux peaking, if extrapolable to future devices.

ELMs have a strong impact on SOL heat and particle transport, and PFC loading. Calculations have indicated that ELM fluxes are concentrated at the low-field side near the outer midplane [34]. Once in the SOL, part of the ELM flux propagates to the outer target, but substantial flux also reaches the inner target, albeit with a time delay because of the difference in the connection length. As such, there is an observable time delay between when the ELM heat flux reaches the outer target as compared to the inner target; in D_α light on NSTX, this delay was between 0.1 and 1 msec, i.e. ~ the timescale for convective transport at the ion sound speed. The variability in the time scale was correlated with ELM size; the larger the ELM fractional energy loss, the smaller the in-out delay time. Thus, the in-out delay time yields insight to the ELM dynamics and underlying SOL transport physics, which will be the subject of future modeling with BOUT++ and M3D.

A leading concern about ELMs is the high levels of transient heat flux observed at the PFCs [134]. Measurements of the ELM heat flux have been made in a number of devices, including NSTX. While the inter-ELM heat flux reached 15 MW/m^2 in NSTX, transient ELM heat flux peaks up to 100 MW/m^2 were observed [35]. The peak heat flux increases depended on ELM type [135]. Small type V ELMs resulted in $\leq$ 50% transient increase in peak heat flux. During Type III ELMs, the peak heat flux increased by up to 300% relative to the inter-ELM heat flux, and the heat profile width decreased as compared to the inter-ELM width. The peak heat flux was observed to increase by up to 1000% during type I ELMs, with a significant contraction of the profile width. All of the different types of ELMs exhibited a trend of decreasing profile width

with increasing ELM amplitude. Indeed this last observation is in disagreement with measurements on JET, ASDEX-Upgrade, and DIII-D, and is receiving renewed interest through the ITPA toward resolution of this discrepancy. A recent emphasis in NSTX data analysis is the quantification of the degree of toroidal asymmetry of the ELM peak heat fluxes, the first such detailed study reported in the literature. It was found that larger ELMs have a higher degree of toroidal asymmetry, and also higher toroidal peaking factors [136].

While the emphasis of NSTX-U research will be on ELM control, there are several basic physics studies that will help optimize the control techniques:

- Small ELM physics: research will focus on identification of the underlying instabilities for Type V and Type II ELMs. Various observations have led to a hypothesis that Type V ELMs are resistive instabilities originating from the foot of the H-mode pedestal. This will be tested in NSTX-U (if Type V ELMs are observed in operational scenarios), and comparisons will be made with 3-D stability and transport codes, e.g. M3D-C1 [154] and XGC1. If Type II ELMs are observed in NSTX-U, detailed cross-machine comparisons will be made with higher R/a devices, which show a wider operating window for Type II ELMs than observed in NSTX.

- Large ELM stability: edge stability analysis as a function of the Type I ELM cycle will continue in NSTX-U, looking for ELM onset and violation of PBM stability thresholds. The higher aspect ratio of NSTX-U (R/a ~ 1.7, vs. typically 1.4 in NSTX) is expected to lead to a higher instability drive from the pressure gradient term, as compared to the edge current. On the other hand, the lower ν^* will lead to higher bootstrap current, which is de-stabilizing in the first stability regime unless it opens up access to second stability. The higher spatial resolution of the NSTX-U profile diagnostics will facilitate the assembly of the kinetic profiles needed for construction of kinetic equilibria that will be used for evaluation with the ELITE code[22].

- Distribution of ELM heat fluxes on PFCs: research in NSTX focused mainly on ELM heat fluxes to the lower divertor, due to the need for fast IR thermography. In NSTX-U, this research will be expanded to the upper divertor , center stack, and outer wall, as double-null and marginally diverted configurations will be evaluated with an expanded thermography diagnostic set. In particular, the observation of contraction of the heat flux profile with ELM increasing ELM size will be evaluated and compared with other devices, which typically report a 20-50% increase in ELM heat flux footprint for large Type I ELMs. Measurements in NSTX-U will be compared with simulations from XGC0 and XGC1.

- Correlation between ELM heat flux and resulting erosion evaluated with spectroscopy will be initiated.

The role of SOL current (SOLC) in ELM stability will also be investigated. SOLCs are defined as electrical current driven along field lines by thermoelectric potential when the electron temperature is different at the two ends of open field lines in the SOL [50]. These SOLC have been observed to coincide with ELM onsets on NSTX. It has been hypothesized [51, 52] that SOLC provide a key unifying physics element underlying the complete ELM cycle, consisting of triggering, edge thermal collapse, and relaxation, the physics of which remains elusive in spite of the success in creating H-mode discharges free of intrinsic ELMs and in generating ELM-like edge thermal collapses in an otherwise ELM-free discharge. Measurements of the SOLC during ELMs will be made in NSTX-U, and it is anticipated that the study of SOLC current under ELM paced condition will aid in understanding the physics mechanism in the triggering of ELMs. Ultimately manipulation of SOLC will be evaluated as an actuator for ELM control.

4.2.1.2.2 Pedestal Structure

Substantial progress has been made in pedestal physics over the last decade, particularly with development of several pedestal structure models [16, 17]. One leading theory on the physics limits to the pressure profile is the EPED model; this model employs a local pressure gradient limit due to kinetic ballooning modes (KBM), and an overall pedestal height/width limit due to PBM. As described above, violation of PBM stability is thought to destabilize ELMs. While the EPED model compares well with data from high aspect ratio devices, extension of the KBM calculations to low R/a is still in progress, noting recent work in this area from the MAST device [18]. A second pedestal structure model that places limits on the individual density and temperature profiles is the 'paleoclassical' model, in which poloidal magnetic flux diffuses radially and resistively in thin annuli, carrying charged particles [19]. This model reproduces many of the characteristics of the profiles in the steep gradient region near the separatrix. Finally a third pedestal structure model considers the effects of the X-point topology and scrape-off layer on neoclassical (XGC0) and turbulent transport (XGC1), including both recycling and kinetic effects. These pedestal structure models are complemented by interpretive models to determine the cross-field transport needed to reproduce observed profiles (e.g. SOLPS, UEDGE, OEDGE), and stand-along turbulence codes (e.g. BOUT++, SOLT).

In NSTX, comparison of pedestal structure data with the two pieces of the EPED model, namely KBM and PBM, have been promising. These comparisons were made in both ELMy [20] and ELM-free discharges [7, 8, 9]. Figure 4.2.2 shows evolution of the pedestal height, width, and maximum gradient as a function of normalized ELM cycle duration. Panel 4.2.2a shows pressure pedestal height saturation prior to the onset of ELMs in low and intermediate plasma current. At high current (> 1MA), a continuous increase of the pedestal height is clearly observed. Panel 4.2.2b shows that the pedestal width is observed to grow during the ELM cycle. The pedestal pressure gradient, however, is clamped (panel 4.2.2c) within the first 20% of the ELM cycle,

suggestive of a transport process regulating the gradient. Initial characterizations of the fluctuations between ELMs clearly point to the existence of ion-scale turbulence possibly responsible for the transport in the pedestal region [21].

In these ELMy discharges, the pedestal width appeared to scale almost linearly with β_θ^{ped} (see Figure 4.2.3) [20], rather than as $[\beta_\theta^{ped}]^{1/2}$, as observed at higher aspect ratio [22]. The square root dependence at high aspect ratio originates from KBM physics. A preliminary KBM calculation for NSTX indicates a width $\sim (\beta_\theta^{ped})^{0.8}$, i.e. the faster than square root scaling appears to be a low R/a effect [23]. In contrast, MAST found [143] a pedestal width dependence as $[\beta_\theta^{ped}]^{1/2}$; the reason for this apparent discrepancy will be investigated via collaborative studies between NSTX-U and MAST-U, with improved diagnostics on each device. Other theoretical models of the pedestal width are also being evaluated. One such model predicts that Electron Temperature Gradient (ETG) modes are dominant in the pedestal, leading to a
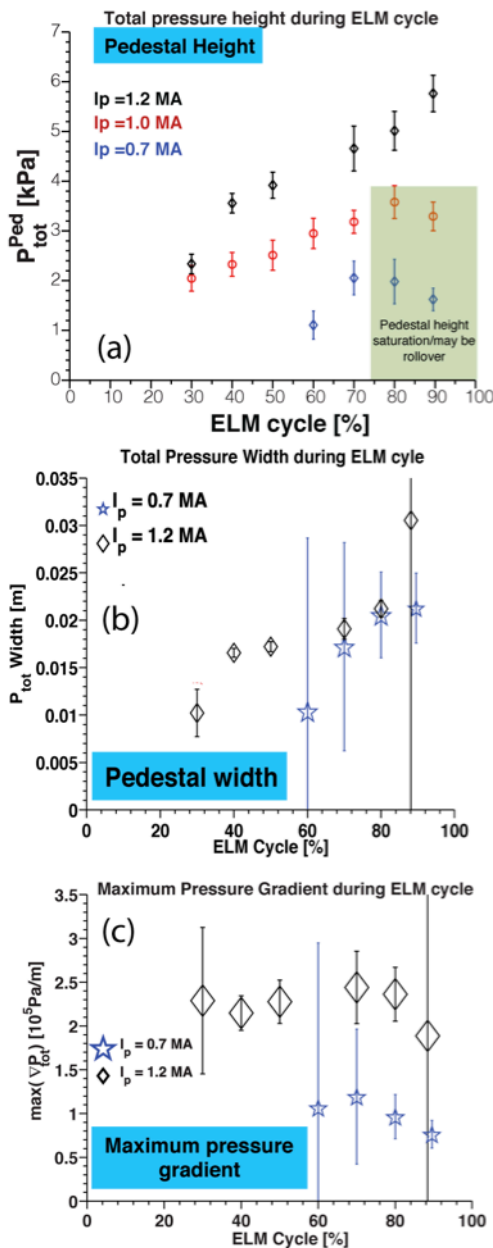

Figure 4.2.2: Shown to bottom the evolution of (a) the pressure pedestal height, (b) the pressure pedestal width, and (c) the pressure maximum gradient.
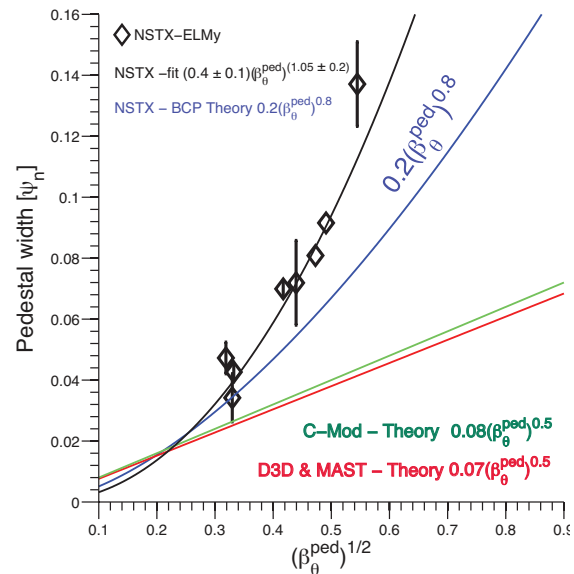

Figure 4.2.3. Pedestal width scaling with predicted width scaling using BCP.

near linear scaling of the pedestal width with β^{ped}

4.15

[24].

The use of lithium conditioning radically altered the pedestal structure in NSTX, which was thought to be critical in the observed ELM elimination [7,8,9,44]. The density gradient in the recycling source region from $0.95<\psi_N<1$ was reduced proportionally to the reduction in core fueling from lithium pumping of deuterium at constant cross-field particle transport. However the n_e gradient radially inward of the recycling source region from $0.7<\psi_N<0.95$ was increased relative to the reference discharges, indicating a substantial reduction in cross-field particle transport. This region of improved particle transport correlates with an improved region of electron thermal transport that exhibited much larger T_e and P_e gradients that the reference discharges.

Despite the good progress made in characterization of the NSTX pedestal structure, a number of questions remain from the above studies, requiring new data from NSTX-U. Several of these questions are listed below:

- Given that the near linear scaling of pedestal pressure width on pedestal β_θ^{ped} is close to the dependence from the recent KBM calculation mentioned above, and the pedestal pressure gradient clamped early in the ELM cycle, why was there no evidence of onset KBM or any other modes responsible for transport in NSTX or any other device fluctuation data aligned with the ELM cycle? Note that many devices have reported ion scale turbulence between ELMs [137,21] without conclusive evidence of a stiff onset of instabilities with increasing pressure gradient, as predicted by the KBM calculations.
- Use of lithium conditioning produced very wide H-mode density profiles. What was the origin of the particle transport improvement that resulted in these wider density and pressure profiles?
- Following the lithium studies, to what extent is H-mode pedestal evolution determined by the pressure profile, as opposed to the individual density and temperature profiles?

The extended operating range and new diagnostics capabilities in NSTX-U will help to resolve many of the outstanding questions. During the first two years of this Research plan, the parametric dependences of the pedestal structure will be assessed over the expanded range of B_t, I_p, ν^*, and shaping.

Much of the previous analysis on NSTX required many time slices to create composite density, temperature, and pressure profiles, from which equilibria based on the kinetic profiles were generated, as the starting point for stability and gyrokinetic analysis. This technique, however, requires the assumption that equilibria are unchanging for a particular temporal duration or as a function of the ELM cycle. The improved spatial resolution of the profile measurements, notably Thomson scattering for n_e, T_e, and P_e profiles, will reduce the number of individual profiles

needed to generate a high resolution composite radial profile, and the intrinsic assumptions with the generation of such a profile. Additionally there will be enhanced fluctuation diagnostics in the pedestal region, facilitating the search for pedestal-localized instabilities. These diagnostics include the upgrade of the BES system and the addition of the high-k system with enhanced spatial resolution in the pedestal region.

Following the testing of PBM stability and KBM onset physics, extension and benchmarking of the EPED [25] model in NSTX-U will commence. The predictions of the paleoclassical model will also be tested, as will the predictions of pedestal structure with both XGC0 and XGC1. These studies will be supplemented with continued interpretive modeling of the profiles to infer radial transport coefficients in a variety of operating regimes.

4.2.1.2.3. Pedestal turbulence

It is believed that micro-instabilities and the resulting plasma turbulence are partly or largely responsible for transport in the pedestal region, as is the case in the core plasma. Given the success of the EPED model, the KBM in particular is a leading candidate for limiting the pedestal gradient between ELMs. To improve the physics understanding of pedestal turbulence, efforts have attempted to characterize, both experimentally and through numerical simulations, the instabilities present in the pedestal region.

Edge fluctuation characterization has been performed using reflectometry, which indicates radial correlation lengths of 2-4 cm in the pedestal [21]. These measurements were complemented by dedicated fluctuation studies using the BES system, in which pedestal measurements were made during both ELMy and ELM-free (and MHD quiescent periods) [21, 28]. In the ELM-free regime, for instance, These measurements allowed the parametric scalings among pedestal turbulence
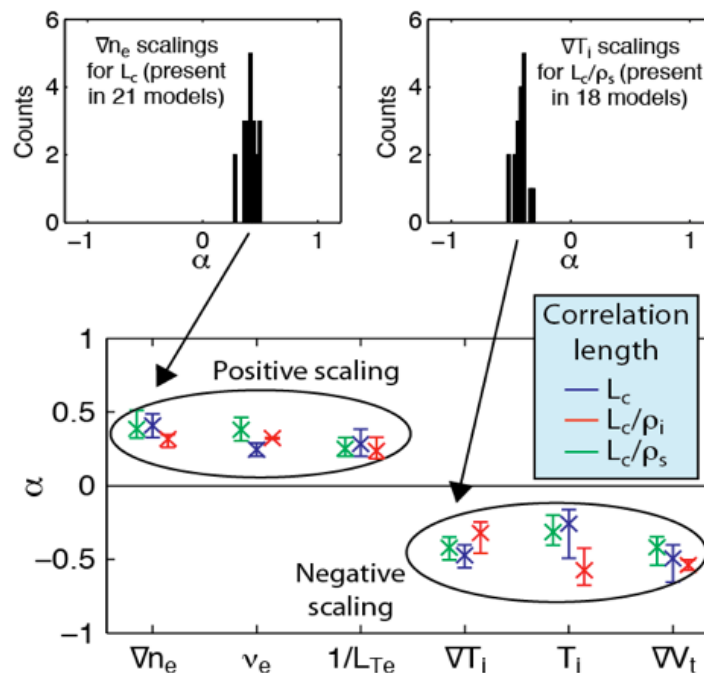

Figure 4.2.4: Regression model aggregation shows poloidal correlation lengths in the pedestal increase at higher density gradient, collisionality, and inverse electron temperature gradient. Similarly, poloidal correlation lengths decrease at higher ion temperature, ion temperature gradient, and toroidal flow shear.

quantities and plasma parameters to be identified [28]. These measurements show broadband fluctuations ($\Delta f \sim 100$ kHz) with poloidal correlation length $L_p \approx 15$ cm and $L_p/\rho_i \approx 10$. Also, poloidal wavenumbers are $k_\theta \rho_i \approx 0.2$ [21, 28] and decorrelation times are inferred to be ~ 5 a/c_s. The observed low-k dependences indicate that the correlation length increases and the wavenumber decreases at higher ∇n_e, lower ∇T_i, and higher collisionality (see figure 4.2.4). Assuming a relation between turbulence characteristics such as correlation length to be related to linear growth rates, the measured dependences appear to agree most with transport driven by TEM, have some agreement with KBM and micro-tearing mode turbulence, but have the least agreement with T_i gradient turbulence.

A number of gyrokinetic codes have been used to characterize edge microinstability in inter-ELM periods, spanning a broad range in the comprehensiveness of the physics included (i.e, linear vs nonlinear, local vs. global, electrostatic vs. electromagnetic, δf vs. full-f). While it is anticipated that a global, full-f, electromagnetic, nonlinear treatment is ultimately required to accurately simulate pedestal turbulence, such codes are still under active development (culminating in the XGC1 code). In the meantime, reduced physics models are used for studying experimental trends; for example local analysis is useful for indicating the types of modes that are present and how they scale with various instability drives (e.g., density or temperature gradients), even though nonlocal effects are likely to be strong in the pedestal and so will quantitatively affect the results [138].

Figure 4.2.5: Profiles of a) growth rate (solid) and ExB shear rate (dashed), and b) real frequency of the most unstable mode without (black) and with (red) lithium.

As an example, a study of the linear gyrokinetic stability of the pedestal was performed using the GS2 code [155]. For a discharge without the application of lithium on the PFCs, these calculations showed that microtearing modes are dominant at the pedestal top (Figure 4.2.5). With lithium applied to the PFCs, the increase in the density gradient in this region stabilized the microtearing modes, and modes with characteristics like those of the TEM becoming dominant with reduced growth rates. In the steep gradient region of the pedestal, ETG modes (not shown) were found to be unstable both without and with lithium, but with higher growth rates and a lower threshold temperature gradient with lithium, suggesting ETG may have played a role in limiting the electron temperature gradient in this region. At mid-pedestal, a hybrid TEM/KBM mode was found to be dominant with and without lithium, with characteristics of both the TEM and KBM [29].
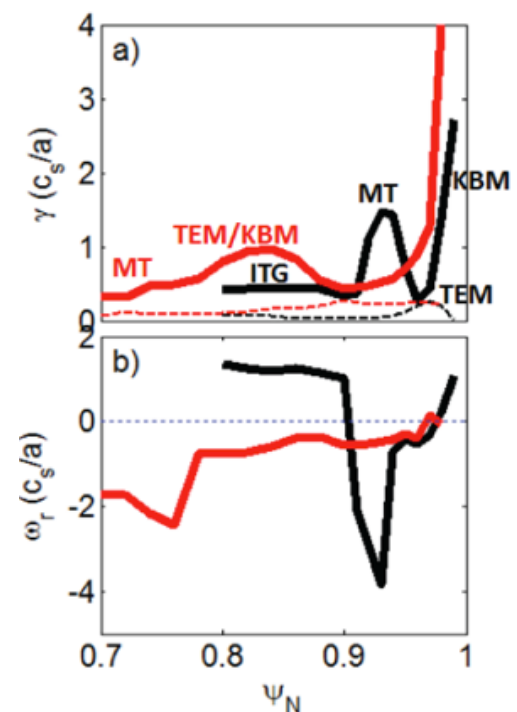
Local gyrokinetic linear simulations have also been performed of a separate set of discharges using the GENE code [156]. A hybrid TEM/KBM mode was identified in the linear GENE simulations[23] during the last 20% of an ELM cycle near the pedestal top, similar to that found within the pedestal using GS2.

Global nonlinear simulations using XGC1 have been performed on inter-ELM periods in these discharges as well, allowing the first comparisons of specific turbulent features between experiment and theory. XGC1 nonlinear global gyrokinetic calculations yielded radial and poloidal correlation lengths of potential fluctuations in the pedestal region that were consistent with those from the measurements of density fluctuations discussed above (figure 4.2.6) [23].

Finally, GEM gyrokinetic simulations [30] of the NSTX pedestal turbulence were performed, based on observed pedestal profiles. The GEM simulations indicate low-k linear growth rates increase at higher ∇n_e and lower ∇T_i, a result consistent with observed correlation length scalings based on BES measurements. In addition, GEM simulations indicate instabilities shift to lower k at higher collisionality, in agreement with observed wavenumber scalings. These dependences indicate, as with inferences from the measurements, low-k turbulence dominated by TEM in this region of these discharges.

Figure 4.2.6: (a) 2D cross-section of the potential fluctuations from XGC1 simulations in the fully nonlinear stage. (b) Zoomed in edge fluctuations indicating the BES and reflectometry measurements region. (c) Evaluations (from simulation) of both radial (4 cm) and poloidal correlation (11 cm) lengths in the edge region showing experimental level radial and poloidal correlation lengths.
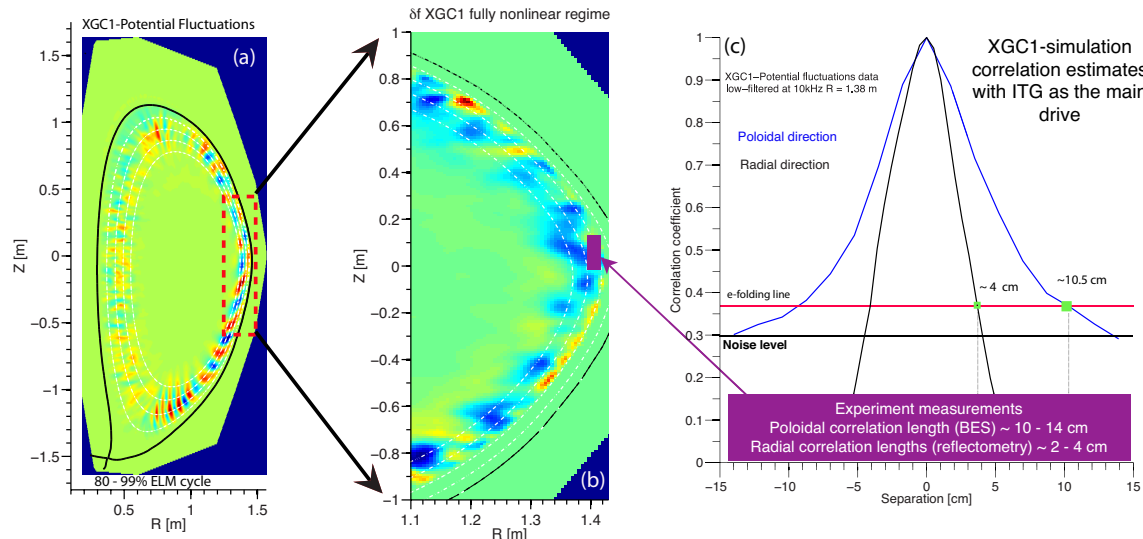
Pedestal turbulence research on NSTX-U will benefit from several diagnostic upgrades. New BES channels will be instrumented, giving expanded 2D spatial coverage of 2 cm by 2 cm in the pedestal region. These will aid advanced analysis techniques, such as velocimetry analysis of

density fluctuations to identify predator-prey relationships between turbulent eddies and flow fluctuations. A high-k_θ microwave scattering diagnostic will also be implemented, and when combined with BES and reflectometry will yield an almost complete range of the k_θ spectrum of fluctuations from ion to electron gyroradius scale lengths. Furthermore, a polarimeter will be installed early in the Five Year research period, allowing diagnosis of magnetic fluctuations as expected due to, e.g., microtearing modes. The pedestal turbulence studies will also be improved by the expanded facility capabilities of NSTX-U. This includes access to a broader range of physics parameters (e.g., $\nu*$), as well as the ability to probe pedestal turbulence as edge conditions are altered using, e.g., wall conditioning techniques or 3D field application.

Gyrokinetic simulations will be continued in the extended operation range of NSTX-U to identify the micro-instabilities present in the edge region, and to develop a model a predictive model of edge transport. Nonlinear simulations will be a focus of this research, in order to directly compare turbulence characteristics to measurements. Of particular importance in these calculations is proper treatment of the larger physical scale lengths in the ST owing to the low B_t, which may demand global rather than local simulations; this is especially true in the pedestal, where the ion gyroradius is not small relative to characteristic gradient scale lengths. The various codes are being continuously developed to both include more physics and to be able to handle the large spatial ranges required for proper ST simulations; for example, GENE and GYRO are capable of the nonlocal electromagnetic simulations needed for the pedestal, and XGC1 will add full-f capability and inclusion of the separatrix and scrape-off layer to this once electromagnetic effects are fully implemented.

4.2.1.3. Active control of ELMs and pedestal on NSTX

It is well-known that steady operation of ITER hinges on achieving acceptable ELM size. To date the commonly utilized approaches in reducing ELM sizes include the radiating divertor, the magnetic triggering via vertical kicks, pellet pacing, and the external resonant magnetic perturbation fields. In NTSX, lithium conditioning of the PFCs has been observed to eliminate ELMs, albeit with increased impurity accumulation typical of ELM-free H-modes. ELM control will continue to be a high-priority research area in NSTX-U.

4.2.1.3.1. 3D Fields ELM pacing

The use of 3D fields for pedestal control was explored in NSTX experiments. In contrast to RMP ELM suppression experiments at, e.g., DIII-D [36], it was found that the application of 3D fields caused ELMs to be destabilized in NSTX during otherwise ELM-free H-modes [37]. This effect was leveraged to perform ELM-pacing for impurity control during NSTX discharges with strong lithium conditioning [37]. While ELM-triggering by 3D fields was robustly observed, the impact

of 3D fields on the pedestal kinetic profiles was found to vary with discharge conditions. For example, in a discharge at low elongation and without lithium coatings on the PFCs, the 3D field caused the pedestal T_e to increase, while in a high elongation discharge with lithium flat spots were measured in the pedestal n_e and T_e profiles without any increase in T_e [38].

In NSTX-U ELM control using applied 3D fields will be explored using the expanded operational range available as well as upgrades to the 3D coils system. In particular, the lower ν^* achievable in NSTX-U will allow contact to be made with $\nu_e^* < 0.2$ ELM-suppression experiments performed on other devices, e.g. DIII-D [39]. Further, it is likely that the transport response will be different at reduced ν_e^* (< 0.12), and a stronger impact on particle transport may be possible [40]. The 3D field system itself will be greatly expanded in NSTX-U, giving a wider spectral range
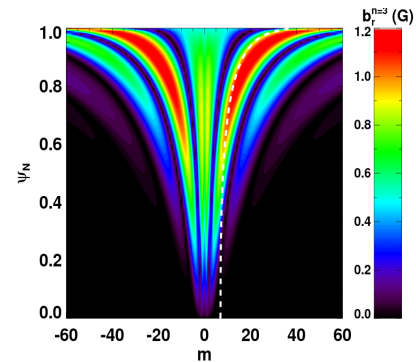

Figure 4.2.7: Poloidal spectrum of n=3 perturbation applied with NCC (dashed white line indicates resonant values)

than in NSTX with more flexibility in resonant vs non-resonant field application. This will be facilitated by the implementation of independent power supplies for all six of the existing coils at the start of NSTX-U operations, and the partial installation of the in-vessel NCC coils towards the middle of the Five Year Plan period. The NCC coils will allow for control over the poloidal spectrum of the applied perturbation, which has been shown to be a key ingredient in achieving ELM suppression at DIII-D [41]. These coils may also allow a substantial increase in the ELM frequency to be achieved during pacing via 3D field application. If so, this could allow very small ELMs to be triggered rapidly in order to simultaneously control the ELM size and particle content of the core plasma.

4.2.1.3.1.1 Projections using the NCC coils

An open question on ELM stability is whether the 3-D fields themselves directly impact ELM stability, or whether the changes to the kinetic profiles can be used in 2-D stability calculations with e.g. ELITE. While 2-D ELITE calculations are consistent with RMPs changing the profiles in a way that improves stability to peeling-ballooning modes [139], very recent analysis suggests that the ELM stability threshold might be reduced by the application of RMPs [140].

The impact of the NCC on ballooning stability has been calculated in order to assess how the new coil set might be expected to alter the pedestal structure and stability. The approach used is described in [38]. First, a 2D equilibrium for NSTX-U was generated with ISOLVER. The pressure and safety factor profile was transferred as input to the 3D equilibrium code VMEC [127], which was then run in free-boundary mode using the same coil currents as in ISOLVER in

order to reproduce the 2D equilibrium. Next, a 3D equilibrium is generated by running VMEC with the same input settings, but with 3D magnetic fields due to the NCC added. The infinite-n ballooning stability of the 3D equilibrium is then analyzed using the COBRA code [128].

The case studied with the NCC applied assumed the full NCC, with two off-midplane arrays of twelve coils each, in an n=3 configuration with even parity (upper and lower coils have the sam toroidal phase). This produces a vacuum perturbation with strong resonant components for the plasma equilibrium under consideration, with much better pitch alignment (Figure 4.2.7) than can be achieved with the midplane coil array alone [37]. Without this field applied, the axisymmetric case is calculated to be stable across the entire plasma radius (Figure 4.2.8, black curves). With the NCC field applied, the VMEC and COBRA calculations indicate a broad region of ballooning instability with 30% of the outer poloidal flux showing positive growth rates (Figure 4.2.8, red curves). For comparison, a case with the midplane RWM coils energized (and not the NCC), again in an n=3 configuration, shows only a narrow edge region (~5% in poloidal flux) that is unstable. This is consistent with the weak impact of the RWM coil set on ballooning stability described in Ref [38]. Similarly a new axisymmetric case, with no 3D fields applied but with the plasma pressure increased by 10%, showed only a small unstable region. Thus, unlike the midplane array [38], the changes to stability caused by the NCC are unlikely to be overwhelmed by small changes in the pressure profile.

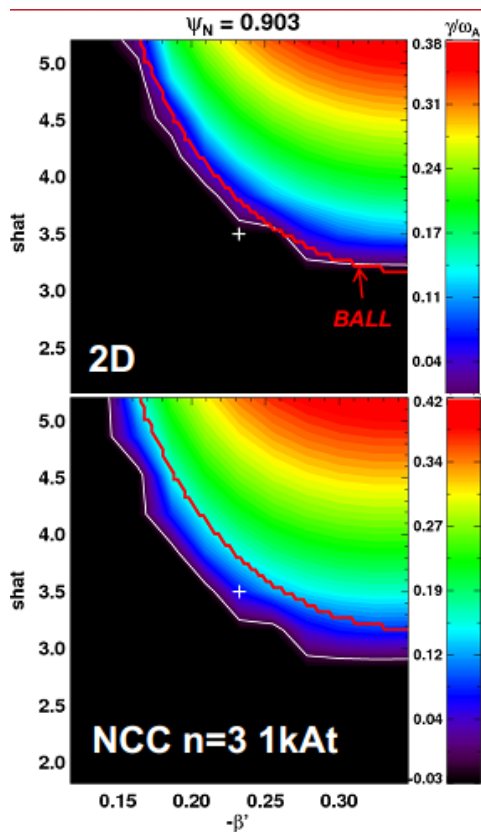Figure 4.2.9: Ballooning growth rates as a function of pressure gradient (-β') and magnetic shear (shat) for a) axisymmetric case and b) with NCC applied. Red curve indicates axisymmetric BALL calculation of stability boundary.
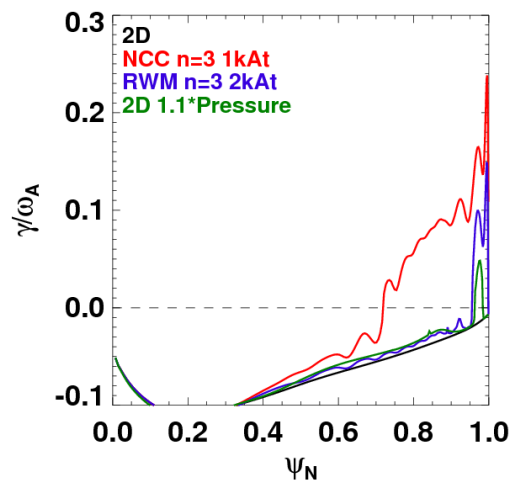

Figure 4.2.8: Ballooning growth rates for nominal axisymmetric case (black), with NCC fields applied (red), with RWM fields (blue), and axisymmetric with 10% pressure increase (green)

To more thoroughly determine the changes to the ballooning stability limits caused by the NCC, large sets of VMEC equilibria were generated with the safety factor and pressure profiles slightly modified near a radius of $\psi_N \sim 0.9$. This allows the stability to be mapped out as the magnetic shear and pressure gradient are varied, similar to the analysis commonly done for axisymmetric tokamaks. Figure 4.2.9a shows the growth rate contours calculated for this set of VMEC equilibria for the 2D case with no perturbations applied. The red contour line indicates the ballooning boundary as calculated from the BALL code, which assumes axisymmetry and uses the 2D equilibrium calculated by ISOLVER (rather than VMEC). The COBRA-calculated growth rate contours closely match the BALL calculation, confirming that the analysis method used here reproduces calculations based on tokamak codes for the 2D case. Figure 4.2.9b shows the same calculation, but now for the case with 3D fields applied (the red BALL curve is again for the axisymmetric case, and is shown for reference). The unstable region extends to lower values in both pressure gradient and shear, so at that the nominal values at this radius (indicated by the white plus sign) the 3D case causes a transition from stability to instability. These results show that the NCC moves the stability boundary by ~20% in pressure gradient, and ~10% in shear, implying that strong changes in growth rates can be expected if the 2D plasma is relatively near the ballooning boundary to begin with. This has been confirmed through calculations for a set of 2D equilbria with the safety factor and pressure varied, which show that the NCC causes wider regions of instability and higher growth rates the nearer the 2D case is to the ballooning limit to begin with.

Since the H-mode pedestal is typically near stability limits, the NCC is likely to have a strong effect. Although the infinite-n ballooning analysis here does not directly affect ELM stability (which requires finite-n peeling-ballooning calculations), it does at least indicate that a strong 3D effect on stability is possible. Further, since ideal ballooning appears to be a good indicator of KBM onset, it is possible that the NCC may be able to alter KBM stability and hence the inter-ELM pedestal structure. These possibilities will be explored experimentally in NSTX-U (while the full NCC has been considered so far, analysis of the partial NCC available early in NSTX-U operation is underway).

4.2.1.3.2. ELM pacing with Li granules

Another method for controlling ELMs has been to introduce high-speed deuterium pellets into the pedestal [42]. It has been demonstrated that as the pellet frequency increases, the amplitude of the induced ELMs decreases and the heat flux to the divertor is reduced. The maximum injection frequency is 90 Hz for the present deuterium pellet injector on DIII-D. A new device (as shown in figure 4.2.10) utilizing Li granules injected via a rotating impeller was developed at

PPPL and recently installed on the EAST tokamak. At frequencies of 25 Hz, the pellets of ~ 0.7 mm in diameter triggered ELMs with almost 100% efficiency as shown in figure 4.2.11 [43].

A new granular injector is presently being fabricated. It will have four selectable sizes of Li granules and be capable of injecting up to 1000 particles/sec with velocities up to 100 m/s for the full five second discharge duration for NSTX-U. One of the main advantages of using Li granules compared to deuterium pellets is that lithium is redeposited on the wall, and is not an uncontrolled fuel source. A second potential application of the Li granular injector is in continuous wall conditioning for long pulses. The injector is capable of supplying over 100 mg of Li per second into the plasma edge. Li coatings from the LITER evaporators have a finite erosion lifetime; the injector can provide a real-time re-supply of Li for wall conditioning. A second granular injector was provided to RFX for wall conditioning studies
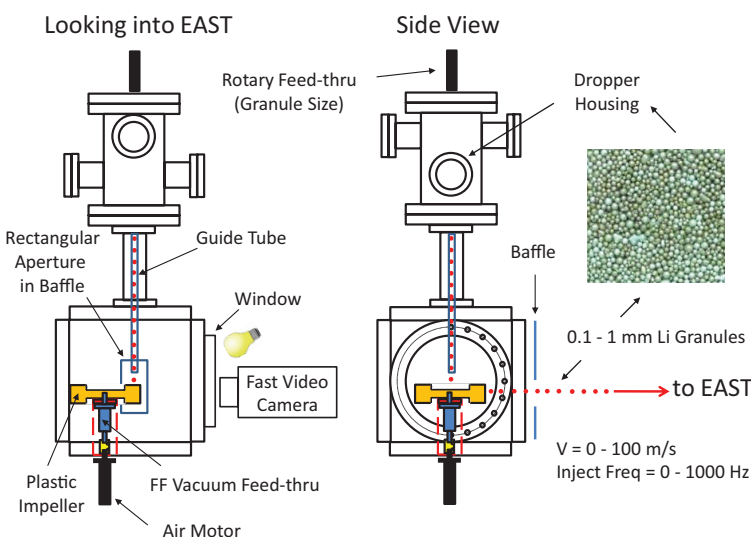

Figure 4.2.10: Two views of the injector hardware used in this work. Pre-sorted spherical Li granules falling through a narrow guide tube were struck by the blade of a rotating plastic impeller. The granules were thus redirected horizontally at higher speeds through a rectangular aperture in a copper baffle and into the midplane of EAST H-mode discharges. Monitoring of the granule/impeller impacts as well as the subsequent granule ablation was accomplished with a fast video camera.

and signs of improved performance were seen at the end of their 2012 campaign.

The physics of ELM triggering by pellets has been investigated with the JOREK code [141], and is in good qualitative agreement with observations on DIII-D. Quantitatively the computed pellet size needed to trigger a ballooning mode is several times larger than observations. The excellent diagnosis of edge filaments with visible imaging and the availability of this granule injector will allow NSTX-U to make significant contributions in model validation in this area.

4.2.1.3.3. Lithium Evaporation control of ELMs

As discussed above, lithium conditioning was been shown to reduce edge recycling, suppress ELMs, and improve performance in NSTX [44]. It was observed that the continuous introduction
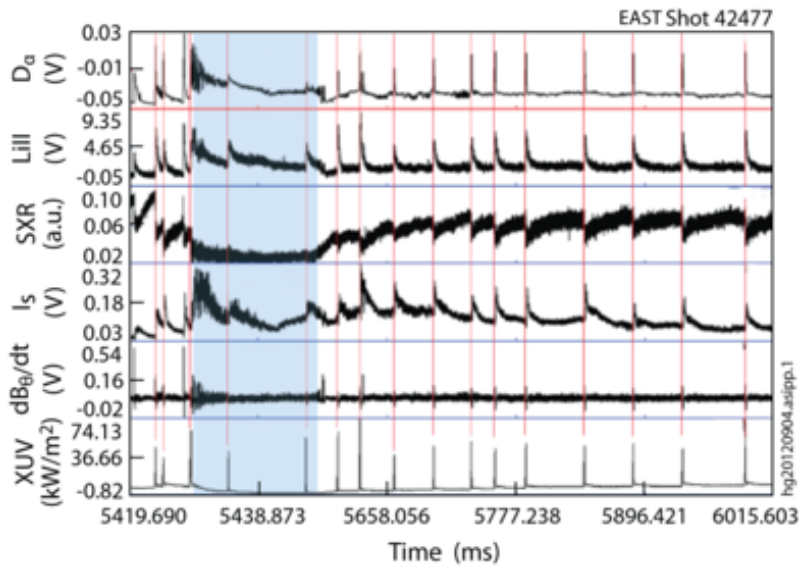
Figure 4.2.11: Shown from top to bottom are signals of divertor Dα, LiII emission, edge soft X-ray emission, divertor ion saturation current, edge Mirnov signal and tangential edge XUV emission. The arrival of injected Li granules is indicated by red vertical lines landmarked to the leading edge of the XUV signal on the bottom. A dithering H to L transition occurs coincident with the injection of the third granule – blue area. After 100 ms, the H-mode returns and a period of 25 Hz ELM pacing driven by the arrival of Li granules at 52 m/s begins.

of lithium coating on the PFCs provides a reduction of the ELM frequency until complete suppression. With increased beam power, B_t, and I_p (all of which are expected to affect ELM stability), NSTX-U will provide a test-bed for the effects of the lithium conditioning on ELM behavior and plasma performance, needed to assess its applicability for next step devices. Finally the effectiveness of more spatially complete lithium conditioning of the PFCs, by implementing an upward facing lithium evaporator (2015) to complement the downward facing evaporators, will be evaluated in NSTX-U.

4.2.1.3.4. ELM pacing using vertical kicks

ELM pacing with vertical kicks had been demonstrated in a number of tokamaks including NSTX [49]. This active ELM control approach has also been demonstrated in ITER-relevant type I ELM regime in ASDEX-U suggesting that this approach may be used for ELM mitigation in ITER. Note, however, that the triggering mechanism is not well understood, and experiments in NSTX-U will be used to improve this physics understanding. With the expanded operational regimes available, NSTX-U will also enable the test of this scheme in scenarios relevant to FNSF.

4.2.1.3.5. Control of ELMs via operational regimes

Two potentially attractive operational scenarios for NSTX-U for controlling ELMS are the Enhanced Pedestal (EP) H-Mode and the I-mode.

The EP H-mode [53, 54] is an attractive regime identified in NSTX experiments, with energy confinement enhancement factors up to $H_{98y2} \sim 1.7$. The EP H-mode usually results from a second confinement transition that occurs following the L-H transition, typically triggered by an ELM (which can itself be triggered using 3-D fields). During the EP H-mode, the pedestal T_e and T_i are significantly (up to nearly a factor of two) higher than in standard H-mode (as shown in figure 4.2.12), while the pedestal density gradient is slightly relaxed. This suggests a separation between the thermal and particle transport channels, and the observed increase in particle transport is promising for achieving stationary densities during EP H-mode. The focus of EP H-mode research in NSTX-U will be on developing techniques to obtain and sustain the EP H-mode. EP H-mode phases that occur shortly after I_p flat-top often terminate in a disruption. To avoid this, β_N feedback control will be used to reduce the power during the EP H-mode. Lithium conditioning will also be used to avoid ELMs during the EP H-mode phase (when an ELM occurs during EP H-mode, the plasma transitions back to a standard H-mode). The application of 3-D fields during EP H-mode will be explored, as it may be necessary to further increase particle transport during EP H-mode to achieve fully stationary conditions.
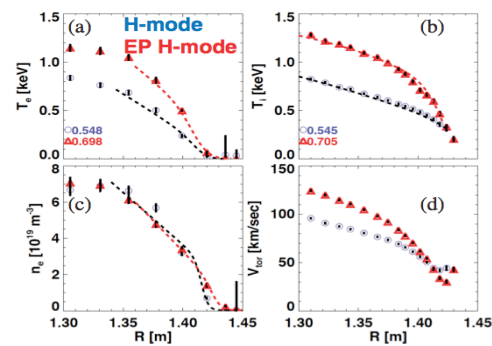
Figure 4.2.12: Profile comparison between Enhanced Pedestal H-mode and H-mode.

The I-mode is also characterized by the presence of an edge thermal transport barrier and the absence of an edge particle transport barrier. The I-mode operational regime is distinct L, H-mode, or EP H-mode and was first observed on ASDEX-Upgrade, and then studied in-depth in the Alcator C-Mod [55]. This regime allows for high confinement and high pressure but without ELMs and without impurity accumulation. While the I-mode regime is an attractive scenario, it has not yet been observed on low aspect ratio tokamaks, such as NSTX or MAST. If such a mode can be obtained, its access conditions and dynamics will be assessed to determine its relevance for both achieving the overarching programmatic goals of NSTX-U and as a possible mode of operation for FNSF.

4.2.1.3.6. External control of particle using EHO Antenna (incremental funding)

It would be highly desirable if particle transport in the pedestal could be externally controlled, perhaps in a finer manner than by driving rapid ELMs. It may be instructive to note that the

ELM-free operation attained in NSTX bears some similarity to the Quiescent H-mode (QH) seen on DIII-D [45] and reproduced on AUG [46], in that ELMs are suppressed in all three cases, in part by operating in a low-recycling regime. A difference, however, is that the electron density and impurity content saturate rapidly in DIII-D and AUG, rather than rising continuously, as in NSTX. The saturation is attributed in DIII-D [47] to the presence of Edge Harmonic Oscillations, EHOs, which appear to increase the particle transport in the pedestal.

In ELM-free lithiated discharges in NSTX, EHOs have recently been observed [48], most clearly in cases with small low-n core MHD activity. These modes are at lower frequency than those observed on DIII-D and AUG, but exhibit a similar harmonic structure. The amplitude of the EHOs on NSTX was less than observed on DIII-D, and at these levels they did not appear to redcue particle confinement on NSTX. The possibility of driving these modes using audio-frequency currents in the NSTX High Harmonic Fast Wave antenna system has been investigated. If successful, this could allow a very attractive new operational regime satisfying the needs for simultaneous avoidance of large ELMs and sufficient particle transport to maintain high-purity, stationary plasma conditions

4.2.1.4. Summary of Research Plans by Year
Years 1-3 (Year 1: 2014):

- Assess the L-H threshold power dependence over expanded parameter range, particularly at higher I_p, including also the effects of geometry and recycling
- Measure the ion and electron turbulence leading up to the L-H transition, and in standard vs. snowflake configurations to compare with predator-prey models and other models of the transition
- Characterize the ELMy regimes in NSTX-U operating scenarios, including access to standard Type I and small ELM regimes, and evaluate the applicability of the EPED model to describe pedestal evolution
- Measure the H-mode pedestal structure (heights, widths, gradients) and pedestal turbulence over the expanded range of both engineering (e.g., I_p, B_t) and dimensionless parameters, in standard and snowflake divertor configurations (see thrust BP-2, section 4.2.2); of special interest are higher I_p (impacting ballooning stability) and lower ν_e^* (affecting micro-stability drive)
- Compare enhanced pedestal turbulence measurements with gyrokinetic calculations
- Assess edge stability of large and small ELM regimes via peeling-ballooning calculations, evaluating if lower ν_e^* causes the computed bootstrap current via Sauter formulation to be in better agreement with XGC0 formulation
- Evaluate the role of resistive MHD in small ELM regimes by comparing data with calculations from BOUT++ and M3D

- Assess the impact of lithium wall conditioning on modifying the edge density profile and ELM stability, in two regimes: where ETG is expected to clamp the T_e profile, and where it is not; assess the efficacy of diamagnetic stabilization in stabilizing peeling/ballooning modes
- Re-establish parameter regime for observation of EHO on NSTX-U, and complete diagnostic studies on their properties
- Investigate the access to EP H-mode, I-mode operational regimes
- Utilize the LGI for ELM control, and initiate collaboration to investigate the physics of the ELM triggering via the JOREK code
- Evaluate the utility of vertical jogs for ELM pacing
- Determine if the midplane coils can be used to alter ELM stability and pace ELMs, and evaluate the peeling-ballooning stability of the triggered ELMs
- *Incremental: begin to design and construct power supplies to drive EHOs*

Year 4-5:

- Compare effect of cyro-pumping (see thrust BP-3, section 4.2.3) on pedestal structure and turbulence with lithium and boron coated PFCs
- Evaluate the impact of high-Z PFCs on the pedestal performance
- Evaluate the compatibility of high-Z PFCs with ELM control tools developed in the first years of the Plan
- Evaluate the ability to control edge particle transport and ELM stability with the NCC coils, and compare with 3-D ballooning calculations
- Combine the new particle control tools (cryo-pump and LGI) to trigger ELMs on demand while maintaining the pedestal structure for maximum fusion performance
- *Incremental: Demonstrate EHO drive and make preliminary measurements of the effects of driven EHOs on pedestal and SOL transport*

4.2.2 Thrust BP-2: Control divertor heat fluxes with a combination of innovative and proven techniques

The discussion of this thrust is broken into two subsections below: edge/SOL transport and turbulence that likely set the upstream heat flux channel, and innovative and conventional methods to control the divertor heat fluxes.

4.2.2.1 Edge/SOL physics

Edge and SOL plasma physics is important since it determines edge gas fueling efficiency and pumping, impurity screening (the influx and redeposition of impurities), and the performance of

RF heating systems. The basic processes that determine the edge and SOL parameters in present and future tokamak-like devices, however, are not yet well understood. The present section, therefore, focuses on fundamental plasma physics issues of the edge and SOL which will be important for *all* operation modes or divertor configurations of NSTX-U, or for any future tokamak-like device including ITER and/or an FNSF. The goal of the research in this section is to obtain a better fundamental understanding of the edge/SOL plasma and to use this understanding to improve and develop new techniques to control edge heat and particle flows.

4.2.2.1.1. Plasma transport and flows in the edge/SOL

Understanding of the inter-ELM heat transport in the tokamak SOL is critical for projecting divertor conditions in ITER and ST-FNSF. In 2010, the US community investigated SOL thermal transport and scaling via a national Joint Research Target (JRT) on SOL thermal transport. In this work, the three large US facilities, C-Mod, DIII-D, and NSTX, collaborated to develop common datasets and analysis techniques on divertor heat flux profiles over a wide range of collisionality ν^*, beta β, parallel heat flux $q_\parallel$, peak heat flux, and divertor geometry. In particular, the width of the divertor heat flux footprint λ_q^{div} is a critical parameter in projecting the peak divertor heat flux: at constant exhaust power, λ_q^{div} and the peak divertor heat flux q_{peak}^{div} are inversely related [4]. In low-medium recycling conditions, the divertor heat flux channel λ_q^{div} can be related to the midplane heat flux width in the SOL, λ_q^{mid} or simply λ_q, approximately through flux expansion[56,57]. Individual studies and regression analysis of the joint dataset showed λ_q decreasing $\sim 1/I_p$, with an additional notable dependence on minor radius. Very importantly, there was little or no consistent major radius R, B_t, or heating/loss power dependence. This result was affirmed when the U.S. dataset was combined with European data through the ITPA. Because of the a/I_p dependence, it was more appropriate to compare λ_q^{mid} across devices using the poloidal magnetic field at the outer midplane, $B_{pol, MP}$. As shown in figure 4.2.13, the scaling of the inter-ELM λ_q^{mid}, under attached divertor conditions is given
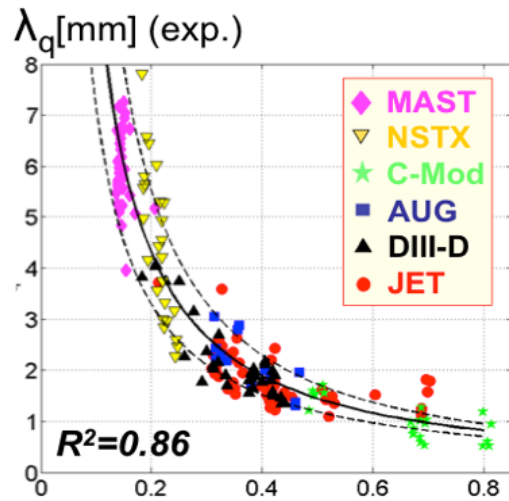

Figure 4.2.13: Multi-machine scaling of the scrape-off-layer width at midplane.

approximately by [157]:

$$\lambda_q^{mid}(mm) = (0.63 \pm 0.08) \times B_{pol,MP}^{-1.19}$$

The projection for ITER under these conditions would be $\lambda_q^{mid} \sim$ 1mm, which is 70-80% less than the present design assumption. Radiative divertor operation, i.e. near partial detachment, will be necessary for ITER and FNSF, where dissipation of large $q_{\parallel}$ will be required for successful operation and protection of PFCs. Thus new ITPA studies are beginning to address how these dependences change with higher recycling and radiation. Upon commencement of operation, NSTX-U will contribute to these studies, and also attempt to resolve the relatively large variability in spherical tokamak data (i.e. MAST and NSTX in figure 4.2.13) with respect to the scalings.

Additionally in NSTX research, it was found that lithium wall coatings decreased λ_q^{mid} [57] and softened the $1/I_p$ dependence, for which the underlying physics was not determined. These measurements were enabled with a novel two-color IR thermography system [158]. Some basic physics questions that will be addressed by NSTX-U research are:

(a) what dimensionless parameters determine the SOL width in NSTX-U?
(b) what physics mechanisms are responsible for the SOL width scaling?

A neoclassical drift-based transport model, in which cross-field drifts across the separatrix are balanced against near sonic parallel flows in the SOL, was derived, predicting a $\lambda_q^{mid} \sim$ the ion poloidal gyro-radius. Electron turbulent transport is assumed to allow heat flux from the core to fill the SOL, which drains the heat with Spitzer parallel conduction. The λ_q^{mid} prediction from this model $\sim (a/R)\rho_{pol}$, and is in remarkably good agreement with experiment, as shown in figure 4.2.14 [5, 58].
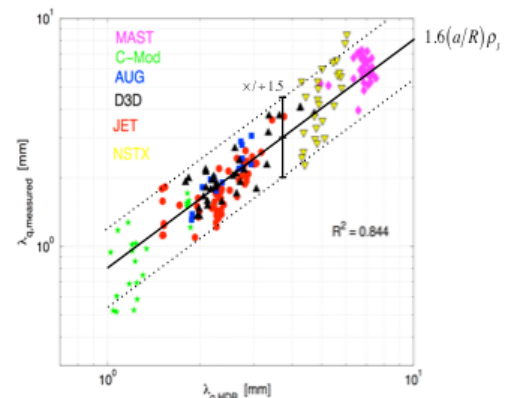
Figure 4.2.14: Comparison of experimental data with heuristic drift-based model.

The derivation of the model is heuristic, and therefore requires stronger theoretical and computational justification, which will be pursued with the XGC suite of codes. Key experimental measurements to test the physics underpinning the theory include the flow speeds at the midplane and divertor, as well as possible dependences of λ_q^{mid} on plasma geometric features, such as triangularity and the direction of the ∇B drift. These will be determined computationally, for comparison with new experiments in NSTX-U.

In general, the SOL width is assumed to be set by interplay of radial transport via plasma turbulence and/or neoclassical drifts, and parallel transport on the open field lines. A typical modeling approach is to simulate the SOL plasma with 2-D transport codes that assume enhanced turbulence-induced radial transport to fit experimental plasma profiles. On the other

hand, plasma turbulence simulations indicate that turbulent fluxes of the required magnitude arise from instabilities driven by radial plasma gradients themselves. Since the profiles and turbulence are strongly coupled, a self-consistent calculation requires coupling of simulations for turbulence and profile evolution. Such self-consistent calculations can be performed using e.g., the turbulence codes BOUT++ and XGC1, coupled in some manner to fluid codes like UEDGE or SOLPS.

4.2.2.1.2. Edge impurity transport

The planned studies of SOL/divertor impurity transport are necessary for a validated numerical model, and will have a direct impact on the impurity-seeded radiative divertor program and PFC plans. The edge/SOL plasma is affected by neutral fueling and by impurity sources at the divertor/first wall, thus, making it a complex multi-species, multi-physics problem. Impurities originating from the PFCs due to ion and energetic neutral sputtering, or introduced externally as a seeded gas, recycle at the divertor and wall, with a small fraction penetrating into the confined plasma. Material migration studies are discussed in Chapter 5; here, SOL transport and screening are discussed.

In the main chamber SOL, the near and far SOL zones are dominated by turbulent, often highly convective, cross-field transport. In the divertor chamber, where parallel gradients develop, the impurity retention and impurity pumping efficiency are determined by the classical transport parallel to the magnetic field as well as classical and neoclassical drifts. New NSTX-U capabilities, namely, a range of ν^*, and long pulse, together with a mixed-material environment that includes low-Z (Li, B, C) and higher Z (e.g., Ne, Ar, Mo) impurities, would enable a comprehensive experimental program of impurity migration and transport studies. In particular, the research program in the initial years will focus on lithium and carbon transport, with increasing emphasis on high-Z transport as high-Z PFCs are introduced.

The experiments will be supported by multi-fluid and gyro-kinetic model development and validation. The multi-fluid codes SOLPS and UEDGE will be used for edge transport and plasma-surface interaction (PSI) modeling. The main questions that the fluid modeling can address are (1) comparison of the measured and modeled impurity source strength evolution, shedding light on the erosion processes; (2) parallel and radial SOL transport and plasma fluxes in reduced recycling regimes with lithium coatings. Numerical modeling of impurity transport in NSTX-U edge plasma using the edge plasma fluid turbulence code BOUT++ will also be done. Multiple fluids can be incorporated in BOUT++ plasma model for representing ions with different charge states. This multi-fluid approach will be sufficient for capturing important physics relevant to impurity ion transport, e.g., inward transport by plasma "holes" in the edge. The BOUT++ modeling can be compared with turbulence-resolving diagnostics (e.g., BES, GPI,

fast cameras) and turbulence-averaged impurity profiles measured by filtered cameras and spectrometers. The most comprehensive code available for these comparisons will most likely be XGC1, which should have 3-D geometry, kinetic neoclassical orbit effects, neutral and impurity models, atomic radiation, and an edge/SOL turbulence model. This code can be used to study the interactions between various physics effects, which are coupled, e.g. through the radial and parallel electric fields, which cannot easily be measured directly. In addition, other specialized codes will probably be useful to help interpret the experimental results; e.g., codes which calculate edge neoclassical transport (NEO) [59], edge MHD (M3D) [60], and edge RF coupling (AORSA-2D) [61].

4.2.2.1.3. The 3-D structure of edge/SOL turbulence

The tokamak edge/SOL is a highly turbulent plasma with up to order unity fluctuation amplitudes. A basic understanding of the edge and SOL must include an understanding of the structure of its turbulence, and how this structure changes with externally controllable variables, e.g. B_t, I_p, NBI or RF power, magnetic configuration. The 3-D turbulence structure can be extremely well diagnosed on NSTX-U because of its excellent access for instrumentation, and shaping flexibility to optimize diagnosis. Turbulence and its 3D structure could have a critical influence on the plasma transport and flows in the edge/SOL to be discussed in the next subsection.

The 3-D structure effects on edge/SOL turbulence are particularly important in spherical tokamaks because of the extreme magnetic shaping and flux expansion ratio, and field-line sear in the edge region. For example, a circular magnetic flux tube in the outer midplane SOL of NSTX is "squeezed" into a very thin ribbon by the time it reaches the X-point region, and finally maps into a toroidally-elongated and very thin radial strip by the time it intersects the divertor plate (see Fig. 4.2.15). Thus a circular blob-filament formed at the outer midplane may be inhibited from reaching the divertor plate if its flux tube becomes thinner than an ion gyroradius near the X-point, which could affect both the parallel and cross-field transport effects of the turbulence. The theory of 3-D edge/SOL turbulence is presently under active development using analytic models [62, 63, 64] and computation simulations such as BOUT++[65] and XGC1 [66].

Figure 4.2.15: 3-D visualization of a magnetic flux tube in the SOL of NSTX. A circular tube at the outer midplane (upper left) becomes shaped like a ribbon near the divertor region (bottom).

Some basic physics questions on 3-D edge turbulence physics which can be answered by comparisons with experimental results on NSTX-U are:

(a) where do plasma blobs form and how do they move along/across B field lines?
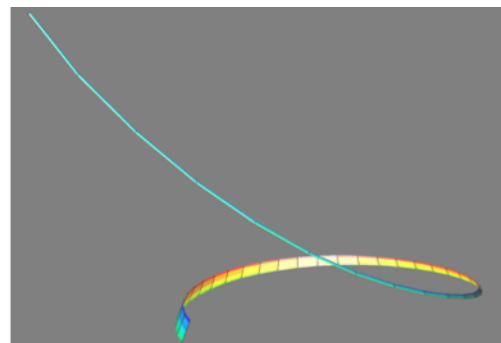
 (b) how does the divertor magnetic geometry affect

the edge turbulence structure?

(c) how do 3-D edge fields (e.g. RF, magnetic) affect the turbulence structure?

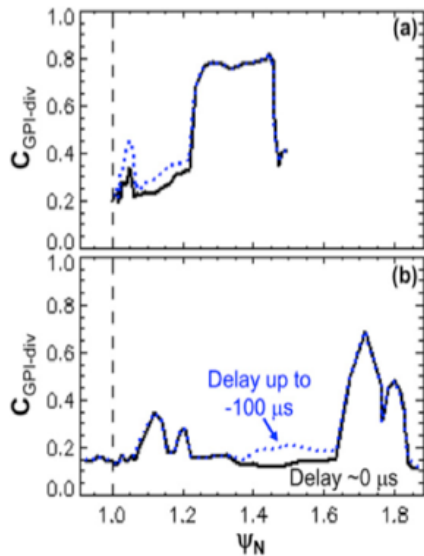(d) how does atomic physics affect the edge turbulence structure?

Figure 4.2.16: Cross-correlation between SOL turbulence seen by GPI at the outer midplane and the divertor plate imaging of Li I light in NSTX [15]. The correlationwas up to 0.8 for both low (a) and high (b) X-point locations.

Note that measurements of the 3-D structure of the turbulence will not allow us to *directly* explain or predict the edge/SOL parameters of present or future devices, since the transport effects of turbulence are a complex function of the fluctuations in density, temperature, and electric fields, which can not be directly measured everywhere. However, the 3-D structure of the turbulence can be compared with the turbulence simulation codes, which then can be used to explain and predict the edge/SOL transport (see also Sec. 4.2.3.3 below). This has already been done at the 2-D level in NSTX using data from the midplane GPI diagnostic and the 2-D edge/SOL turbulence simulation code SOLT [67].

The first activity in this area is to re-establish, and modestly upgrade, the edge/SOL turbulence diagnostics that were previously implemented in NSTX, specifically (a) microwave reflectometry/Doppler backscattering [68], (b) GPI [69], (c) BES [28], (d) divertor Langmuir probes [70], and (e) a divertor fast visible camera [15]. The results of these diagnostics should be compared with each other where they overlap in spatial coverage, e.g. (a), (b), and (c) at the outer midplane and (d), (e) at the divertor plate. An initial picture of the 3-D structure of the edge/SOL turbulence can be obtained early in NSTX-U by comparing the outer midplane and divertor plate results. A start in this direction was already taken by comparing the GPI midplane and divertor imaging measurements [6], which showed a high correlation in the SOL (Fig. 4.2.16).

An outcome of this research program should be a theoretical model for edge/SOL turbulence which has been validated by NSTX-U data. This model can then be applied to predict the SOL parameters and SOL heat/particle width at the divertor plates of future devices such as ITER or FNSF.

Incremental items: this area would benefit from a more complete set of diagnostics to diagnose the 3-D structures. For example, additional GPI views using relatively simple gas manifolds and in-vessel fiber optic bundles can be implemented. Furthermore, divertor probes in the top and

bottom divertor plates can be implemented to examine long-range cross-correlations. Finally a second BES system viewing the second NBI is highly desirable.

4.2.2.2. Divertor physics

Divertor research on NSTX demonstrated that the ST divertor can present both an opportunity and a challenge for the development of the boundary interface [71, 72, 73]. In future ST-based devices, the inherently compact ST divertor that limits volumetric losses, combined with low-collisionality SOL, may result in a sheath-limited divertor operating regime. This regime is characterized by small parallel temperature gradients and results in high divertor heat flux and electron temperature, and puts the divertor concepts to a rigorous test. In NSTX-U, long pulse high power density plasmas will enable divertor research to address the gaps identified for the ST boundary interface, namely, high heat and particle flux control at low normalized density, while also addressing many other boundary physics challenges common to tokamaks [2]. Operation at high divertor loading, e.g. high P/R and P/S as shown in Fig. 4.1.2, will allow NSTX-U to make world-leading contributions because the divertor solutions will be needed for NSTX-U scenarios full power and I_p scenarios. In this section a research program for the NSTX-U divertor heat and particle control is presented.

The present plan for initial NSTX-U divertor PFCs includes passively cooled copper backing plates with 2.5 cm thick graphite tiles. A gradual introduction of high-Z PFCs and lithium deposition methods is planned. Handling high heat fluxes and simultaneously addressing material erosion issues and density control will involve both improved PFCs, and advanced magnetic configurations and radiative solutions. The aim is to develop a boundary interface that can reduce high parallel and perpendicular heat fluxes, from the predicted 400 and 40-50 MW/m^2, respectively, to manageable levels, while maintaining high-pressure pedestal and good core confinement [74].

4.2.2.2.1. Connection to SOL and divertor models and improved diagnostics for model validation.

The goal of NSTX-U divertor research is to characterize heat, ion and impurity fluxes at low ν^* and compare them to edge transport and PSI models to enable predictive understanding of divertor physics for future STs. In the initial years, experiments will focus on comparison of heat flux and neutral/impurity profiles and plasma parameters with model predictions, as functions of power, density/collisionality, and grad-B drift direction.

Closely coupled with the experimental SOL and divertor activities will be predictive and interpretive transport modeling efforts. When SOL collisionalities ν^*_e, ν^*_i are sufficiently high

(10-100), as is the case in the SOL of many present-day tokamaks, a multi-fluid Braginskii transport model can be used, with kinetic corrections for heat diffusivities $\chi_{e,i}$ at the lower end of ν^*. High-performance plasma regimes of future ST-based devices will require lower ν^* than present day devices, thus emphasizing the role of convective heat transport, kinetic transport corrections, and the ion transport channel. Therefore, understanding the SOL and divertor power balance even at a basic level, i.e. how much heat is carried through the SOL to divertor targets through electron and ion channels via conduction and convection, how much power is radiated, would be important for characterizing a particular divertor configuration.

A number of analytic and numerical models will be used to assess heat and particle transport in NSTX-U experiments. Despite their inherent simplicity, analytic models, e.g., extended two-point SOL models [75] or the five-point core-coupled SOL model [76] can often provide physics insights into SOL heat transport, and will be used as a first step in data interpretation. The 2-D plasma transport models, e.g., UEDGE or SOLPS based on multi-fluid Braginskii equations and coupled with neutral transport and PSI models, will be used for more rigorous heat and particle transport analyses. With sufficient constraints provided by the proposed and available profile measurements, parallel and radial transport, impurity migration, and low-recycling regimes can be studied. If warranted by the experimental data and theory developments, the 3-D fluid turbulence code BOUT++ will be used for transport simulations. Radial transport coefficients from the BOUT++ code could be used in UEDGE to enable simulation using cross-field transport based on first principles [77]. Finally, 3-D drift-kinetic XGC0 and gyro-kinetic XGC1 codes will be used to compare with observed experimental trends

Incremental budget item: While the basic suite of edge and divertor diagnostics in NSTX-U, as described in Chapter 10, is extensive and enables numerical code benchmarking and transport studies, a particularly high-priority upgrade is mentioned here, presently included in the incremental budget - a multi-point divertor Thomson scattering system for divertor T_e and n_e measurements. These measurements would be highly beneficial for numerical model validation, e.g. for understanding the pressure/temperature balance between midplane, x-point, and target regions. The divertor Thomson scattering system measurements would also provide critical data for the planned studies of ELM and inter-ELM divertor transport, SOL width scaling, role of X-point heat transport, PSI, divertor impurity transport and spectroscopically-inferred material erosion rates. The data would be also be crucial for the radiative detachment model validation and snowflake divertor transport properties, including the X-point β_p measurements as described below. Initial planning and layout of the divertor Thomson scattering system for NSTX-U demonstrated the feasibility of the laser beam and light collection geometry attractive for high flux expansion magnetic configuration studies.

4.2.2.2.2. Heat flux mitigation in NSTX-U and projections for ST-FNSF

Candidate techniques for steady-state mitigation of divertor heat and particle loads in future fusion plasma devices must be capable of reducing particle fluxes to the levels of acceptable divertor plate material erosion rates and heat fluxes down to $q < 10$ MW/m^2, a limit imposed by the present day divertor material and cooling technology constraints. The techniques must also be compatible with high-performance high-confinement (H-mode) core plasma, high-pressure pedestal, particle control methods, and ELM mitigation techniques. At present, candidate mitigation strategies for ITER and next step fusion devices (e.g., DEMO) include both the passive techniques, such as divertor geometry and magnetic balance, and active techniques, such as radiative mantles, radiative divertors, field ergodization and strike point sweeping [77, 74]. Developed ITER plasma scenarios are based on the radiative divertor: it is planned that both inner and outer strike points will be partially detached immediately after the current ramp up phase and throughout the duration of each discharge. Based on NSTX experiments and modeling, it is planned to focus on two heat flux mitigation strategies in NSTX-U: (1) high radiated power fraction plasmas, including radiative mantles and radiative (detached) divertors, and (2) advanced divertor magnetic configurations.

4.2.2.2.3. Divertor configurations

Advanced divertor geometry configurations take advantage of magnetic modifications of the standard X-point divertor to enhance the geometry effects aimed at reducing parallel and perpendicular (deposited) steady-state and transient heat flux. These effects include poloidal magnetic flux expansion (plasma wetted area), an extended connection length, multiple divertor separatrix branches for power sharing, and increased divertor volume available for volumetric losses. The geometries considered for NSTX-U are the snowflake divertor [79] and the X-divertor [80]; limited work may also be possible on the Super-X divertor [159].

The snowflake (SF) divertor was proposed by Ryutov in 2007 [79] and many of the predicted magnetic and geometry properties have been confirmed in experiments in TCV [81, 82, 83], NSTX [84, 85, 86], and DIII-D. The NSTX experiments, in
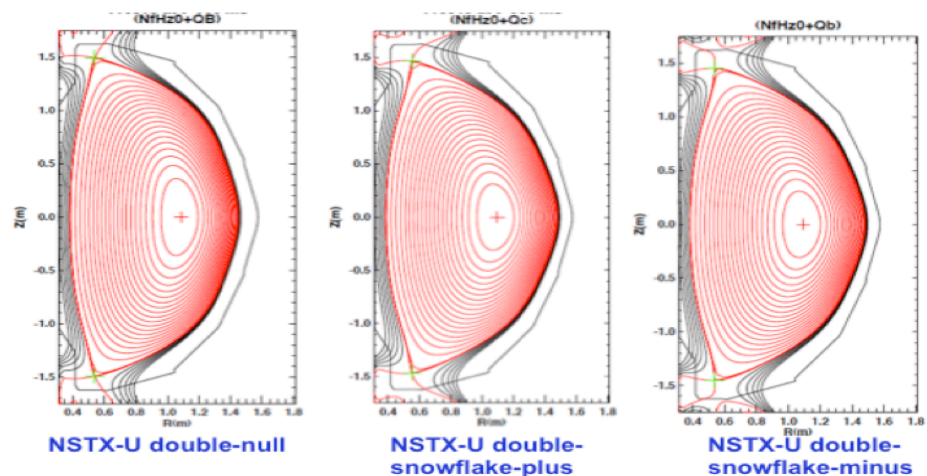

Figure 4.2.17. Examples of modeled plasma equilibria with snowflake divertor

4.36

particular, demonstrated a significant inter-ELM and ELM peak divertor heat flux reduction, reduction of core impurities, and impact on pedestal MHD stability, compatibility with H-mode confinement characterized by acceptable H-mode factors. The SF divertor configuration is considered a leading heat flux mitigation technique for NSTX-U. In NSTX-U, two up-down symmetric sets of four divertor coils will be used to test SF divertors for handling the projected steady-state peak divertor heat fluxes of 20-30 MW/m^2 with $I_p \leq 2$ MA, $P_{NBI} \leq 12$ MW, with pulse length ~ few sec. Magnetic equilibria with SF configurations have been successfully modeled using the ISOLVER Grad-Shafranov equilibrium solver (Fig. 4.2.17) and showed that a robust SF control can be maintained even when time-dependent electromagnetic effects are included. 2-D multi-fluid transport models of the SF configuration have been developed for NSTX-U using the UEDGE code [87]. The modeling projections for the NSTX-U SF divertor geometry are favorable and show large reductions in divertor T_e, T_i, as well as peak divertor heat fluxes due to the geometric and radiation effects, both with 4% of carbon impurity and with neon or argon seeding. The modeling results are summarized in Figures 4.2.18 and 4.2.19. SF divertor solutions high radiation fraction and P_{SOL} up to 12 MW were obtained, with q_{peak} reduced from ~15 MW/m^2 (standard) to 0.5-3 MW/m^2 (SF). The compatibility of cryo-pumping and SF power exhaust were also assessed via simulating a reduced neutral albedo at the cryo-pump duct location (particle exhaust projections are described in the next thrust BP-3, section 4.2.3). It was found that cryo-pumping would reduce divertor density and radiation, resulting in reduced volumetric power and momentum losses. Nonetheless, the heat flux reduction due to SF geometry would still make the SF an attractive heat flux mitigation scenario.

NSTX-U experimental studies of the SF divertor will focus on three areas:
- Development of magnetic configuration control
- Core and pedestal properties
- SOL and divertor transport and radiation between and during ELMs

The focus in the magnetic configuration control and scenario development area in the initial years will be at development of SF configurations and their integration with plasmas of various shaping parameters. Initially only three divertor coils (PF1A, PF1C, and PF2L) will be available for SF control, with an additional divertor poloidal field coil PF1B available in later years if necessary. Equilibria will be developed with variants of SF configurations, including up-down symmetric SF configurations. The modeling will aim to develop understanding of possible configurations, trends and clarify dynamic magnetic flux effects.

In the area of core and pedestal studies in the SF configuration, NSTX-U facility and diagnostic capabilities will enable several novel research directions. The SF configuration is characterized by a larger extent of low B_p region. The associated enhanced magnetic shear just inside the separatrix (w.r.t. standard X-point divertor) may have several important consequences for

boundary physics: (a) The additional local X-point and additional shear may reduce the P_{LH}, as observed in operation in an up/down double-null configuration [142]; (b) energy confinement might increase; (c) pedestal MHD stability of ideal and resistive modes would be affected, in that the increased shear would generally improve edge stability in the first stability regime; and (d) interaction with 3-D perturbations and the modified X-point region would increase prompt ion losses and drive higher E_r [88].

Figure 4.2.18: Projections of snowflake divertor parameters to NSTX-U from UEDGE model. Shown are, for the standard and the snowflake divertors: (a) UEDGE high-resolution numerical meshes with the cryo-pump duct entrance shown in blue; (b) peak divertor heat fluxes and electron temperatures as functions of SOL power; (c) Inner and outer divertor heat flux profiles for the 12 MW input power case; and (d) peak divertor heat fluxes and electron temperatures as functions of recycling coefficient.
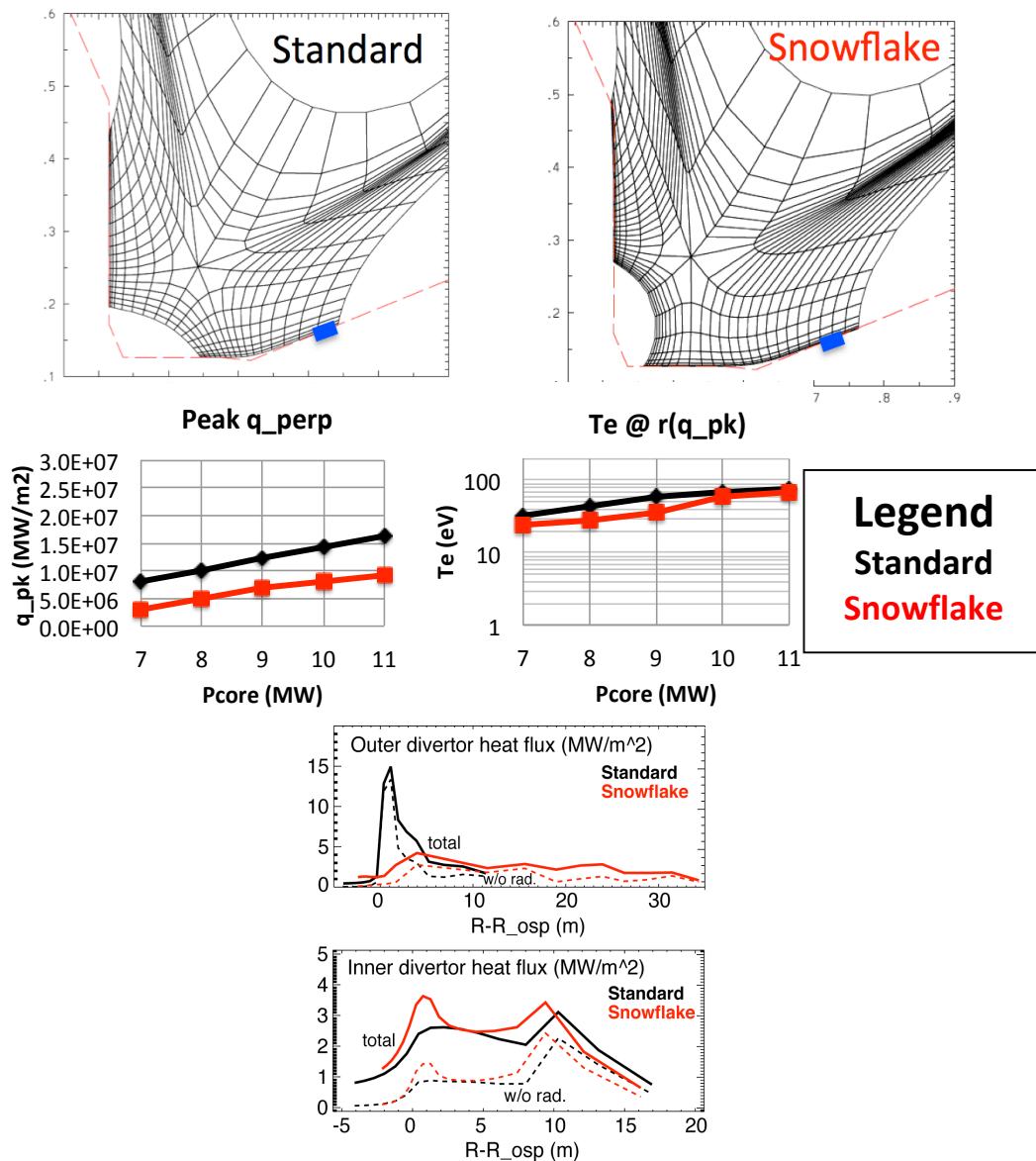
In the SOL and divertor area, the goal is to obtain experiment-based understanding of SF geometry on particle and heat fluxes, so that predictive modeling of the SF configuration for ST-FNSF can be performed. The research will be focused on the comparison of the experimental SF database enabled by the enhanced NSTX-U facility capabilities (e.g. wide range of plasma currents, heat fluxes, different ELM regimes) and multi-fluid models using the codes UEDGE, SOLPS and BOUT++. These comparisons will enable analysis of geometry effects, radiation, ion and impurity transport and turbulence in the SF configurations between and during ELMs [89].

In addition to SF divertor studies and control improvements, evaluation and prototyping of other divertor concepts is envisioned on NSTX-U. These will include the standard up-down symmetric double-null divertor studies and divertor configuration developments. The new divertor coil capabilities may enable experiments with other high flux expansion divertor configurations, e.g., the X-divertor [84, 90]. Pending the outcome of on-going equilibria modeling efforts with the ISOLVER code, experiments presently envisioned for initial NSTX-U years can provide initial tests of stability and heat flux mitigation of these configurations. Collaboration with other facilities, e.g., the spherical tokamak MAST (UK), are also envisioned, particularly toward evaluation of the Super-X divertor configuration.

4.2.2.2.4. Heat flux mitigation based on highly-radiative scenarios

A leading technique for divertor heat load reduction and control via radiated power loss includes increasing impurity radiation fraction to the levels compatible with high-confinement core and pedestal characteristics. The standard operating scenario of the ITER divertor is an impurity-seeded radiative divertor with partially detached inner and outer strike points. In this regime, charge exchange, radiation, and volume recombination are all significant loss channels that bring down peak heat flux. Codes reproduce elements of these processes semi-quantitatively, but do not reproduce the dynamics leading to detachment, e.g. the observation that the inner divertor routinely detaches before the outer, nor do they reproduce the measured SOL flow patterns. Several radiative techniques will be studied in NSTX-U with an aim to improve understanding of divertor detachment process, and develop and demonstrate highly radiative H-mode solutions for ST-FNSF. These techniques will involve radiative boundaries (mantles), radiative divertors with impurity seeding, and lithium vapor-shielding techniques.

In the first two years, basic characterization of these techniques is envisioned, so that further physics-based optimization can be accomplished in later years. These techniques are applicable to steady-state heat flux mitigation, so their compatibility with ELM control or avoidance should also be demonstrated.

Radiative power dissipation at the edge of confined H-mode plasmas (i.e. in the main chamber outside of the divertor) has been demonstrated in several tokamaks, however, its control and scaling have not been studied in detail [91, 92, 93]. High edge radiation fraction scenarios must be compatible with high-pressure pedestal and low core Z_{eff}, therefore, a transport barrier for impurities appears to be a necessary part of these solutions. In initial years of NSTX-U, experiments are envisioned with neon and argon core seeding to provide initial data for evaluation of the concept for ST-FNSF, and further optimization for NSTX-U conditions.

Radiative divertors use deuterium and/or seeded impurities to reduce divertor particle and heat fluxes through volumetric momentum and energy dissipative processes - the ion-neutral elastic and inelastic collisions, recombination and radiative cooling [78, 74]. In NSTX radiative divertor experiments with D_2 and CD_4 seeding, a significant reduction of divertor heat flux from peak values of 4–10 MW/m^2 to 0.5–2 MW/m^2, simultaneously with good core H-mode confinement, has been demonstrated in 1.0–1.3 s discharges [72, 73]. These experiments demonstrated that partial divertor detachment was obtainable in a compact divertor of a high power density ST even with carbon radiation. It is clear, however, that in order to dissipate SOL powers in excess of 5-10 MW in NSTX-U, higher Z impurities (e.g., nitrogen, neon or argon) will be required. Initial multi-fluid edge transport models have been developed for NSTX-U projections with the UEDGE code [87]. The models showed that peak divertor heat flux reduction via partial detachment can be achieved in both the standard and the SF divertor configurations (easier with the latter) in NSTX-U with neon or argon seeding (e.g. Figure 4.2.19). Planned experiments in this area will be critical for further concept development and model validation for ST-based devices that operate at low core and edge ν_e^*.

In initial years, experiments will use open-loop impurity seeding in the divertor. The seeding impurity gas is selected based on operational and atomic physics (radiated power at low T_e) considerations. The seeding gas options will include D_2, CD_4, and Ar in the next five years with graphite and partial high-Z PFCs conditioned via lithium and boron coatings. N_2 is excluded at this stage due to its chemical reactivity with lithium coatings and its absorptivity in graphite. Multi-fluid models will be used for the analysis of power balance and impurity transport in the radiative divertor experiments.

These experiments will set the stage for the radiative divertor feedback control development that would take place in later years. For steady-state high-performance operation, steady-state radiative divertor conditions must be sustained. This can be accomplished by feedback through controlling the rate of injection of the deuterium or impurity gas, using a divertor parameter as a control quantity. The partial divertor detachment was characterized [72,73] in NSTX using a number of divertor plasma measurements: divertor plate surface temperature (heat flux), radiated power using bolometry and impurity emission spectroscopy, neutral gas pressure measurements,

ion flux using Langmuir probes, and divertor recombination using UV or NIR spectroscopy. Based on those NSTX experiments, the control diagnostic signals considered for NSTX-U include divertor radiated power, neutral pressure, spectroscopic deuterium recombination signatures, infrared thermography of PFC surfaces, and thermoelectric scrape-off layer current, as well as spectroscopic "security" monitoring of possible confinement or pedestal degradation

Figure 4.2.19. Projections of radiative divertor solutions for the standard and s=snowflake divertor geometries in NSTX-U from UEDGE model. Shown are divertor peak heat fluxes and radiated powers in the core and divertor as functions of impurity fraction, with neon seeding (a) and argon seeding (b).
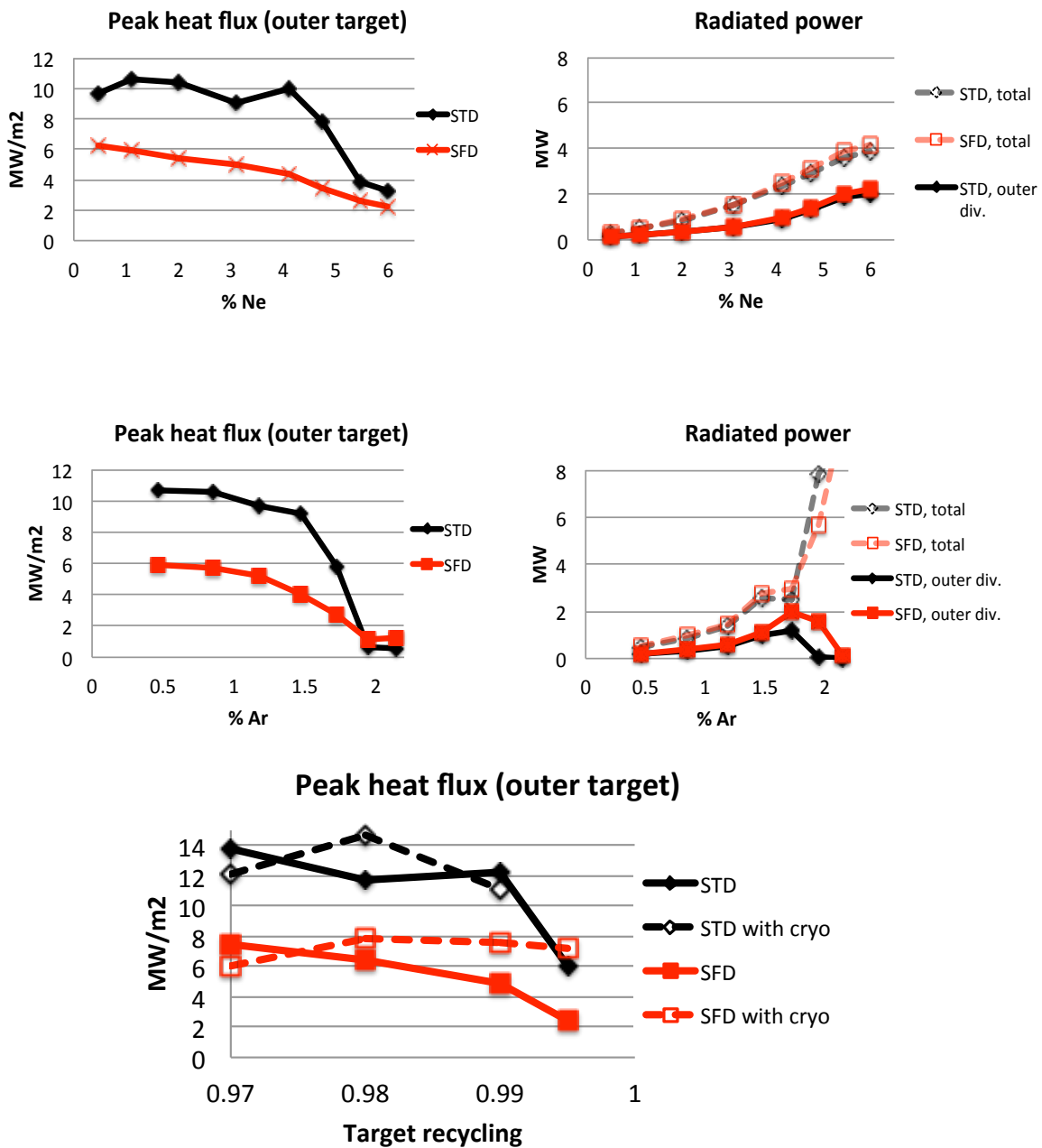
[94].

A prerequisite for radiative divertor feedback control is the cryo-pump that would control the gas inventory. The control aspects of the feedback are described in Chapter 9. The ultimate goal of the radiative divertor feedback control development is a demonstration of a controlled peak divertor heat flux for a long pulse discharge with high performance metrics.

4.2.2.3. Summary of Research Plans by Year

Years 1-3 (Year 1:2014):
- SOL widths, particle/impurity transport, and turbulence
    - o Determine scaling of SOL width vs. appropriate local dimensionless parameters, develop measurement of the parallel SOL flows, and compare with expected neoclassical flows
    - o Measure seeded impurity screening in radiative divertor experiments
    - o Measure lithium, boron, carbon SOL and divertor profiles and assess transport coefficients
    - o Measure the edge turbulence with microwave reflectometry/Doppler backscattering, GPI, BES, divertor Langmuir probes, and a divertor fast visible camera
    - o Compare turbulence measurements where they overlap in spatial coverage, as in previous studies which showed a high correlation of turbulence in the SOL; compare with simulations with the BOUT++, SOLT, and XGC1 codes
    - o *Incremental: perform molybdenum and tungsten injection and screening experiments with a laser blow-off system*

- Snowflake divertor
    - o Develop and test X-point tracking algorithms based on real-time magnetics, and real-time multiple X-point control techniques in PCS
    - o Develop and test up-down symmetric SF configurations, SF formation and disintegration
    - o Evaluate effect of SF on L-H power threshold, edge turbulence and stability, SOL power balance and divertor heat flux, n_e and T_e trends, including detachment onset and characteristics at different n_e/n_G; enhance radiated power with gas seeding (D_2, CD_4, Ne, Ar)

- Divertor studies and radiative divertor feedback control development
    - o Evaluate divertor heat and particle transport as a function of magnetic balance; this will be enabled by new two-color IR thermography of the upper divertor

- o Perform initial radiative divertor studies: measure power balance and operational space (power, density) of the radiative divertor, radiation and recombination spatial distributions, PFC erosion, neutral and impurity retention and compression, MARFE formation and stability
- o Combine radiative divertor with ELM control techniques to keep core impurity concentrations low, if needed

Years 4-5:

- SOL widths, particle/impurity transport, and turbulence
  - o Compare data from NSTX-U with theoretical models/mechanisms (e.g. classical collisional neoclassical phenomena, large-scale convective cells, electromagnetic turbulence, MHD activity) for edge/SOL cross-field transport and parallel flow
  - o Clarify the 3-D edge/SOL turbulence structure *vs.* edge plasma parameters, magnetic divertor geometry, and the presence of 3-D perturbations of various types, e.g. RMP coils, HHFW heating, NBI injection; add GPI views looking down onto the divertor
  - o Continue benchmarking of turbulence models and simulation codes, e.g. BOUT++, XGC1, and SOLT
  - o *Incremental: install a more complete 3-D array of edge/SOL turbulence diagnostics at various poloidal and toroidal angles in NSTX-U e.g., (a) additional GPI views using relatively simple gas manifolds and in-vessel fiber optic bundles, (b) divertor probes at top and bottom divertor plates to look at their cross-correlation, and (c) a second BES system viewing the second NBI.*

- Snowflake divertor
  - o Combine SF configurations with pedestal control scenarios and tools, e.g., the EP H-mode, RMP of various spectra (n=2,3,4) aiming to optimize pedestal structure, transport and stability.
  - o Develop long-pulse discharge scenarios with SF divertor configurations using a full set of all four divertor coils for improved magnetic control, and combine with cryo-pumping
  - o Develop experiment-based model projections for future ST-based devices, such as ST-FNSF, and compare with studies in conventional aspect ratio tokamaks (DIII-D, TCV).

- Divertor studies and radiative divertor feedback control development
  - o Implement radiative divertor feedback control
  - o Demonstrate long-pulse H-mode scenario with feedback-controlled impurity seeding and cryo-pumping

- *Incremental: implement divertor Thomson Scattering to provide critical data for model validation for SF and radiative divertor studies*

4.2.3. Thrust BP3: Compare the sustainability of particle exhaust via lithium pumping and cryo-pumping, for density, impurity, and Z_{eff} control consistent with integrated scenarios

Integrated scenarios on NSTX-U are designed for steady density at 0.5-1 times the Greenwald density limit scaling, and Greenwald fractions as low as 0.35 would be very beneficial to accessing ν^* an order of magnitude lower than NSTX for transport and stability research. To achieve such levels of density control, a central element of the boundary program includes installation of a divertor cryo-pump, representing a proven technology to control both main ion and impurity density. A key component of the research is to compare lithium pumping and cryo-pumping for density control and impurity control. An integral element to both of these studies is the assessment of impurity sources and transport.

Below, the physics design of an in-vessel cryo-pump is described in the first section, as this represents a new, central element of the five-year plan. That is followed by a discussion on the sustainability of pumping via lithium evaporation; liquid lithium PFCs appear only in the incremental budget in this plan and are discussed in the Materials and PFC Chapter. Finally the spectroscopic studies of recycling and impurity sources and transport are described.

4.2.3.1. Cryo-pumping

a. Background
Although the application of lithium coatings on the lower divertor has been shown to be successful in controlling the deuterium inventory of the core plasma in NSTX (see Chapter 9), these plasmas suffer from strong impurity accumulation, leading to a ramping electron density (due to carbon) as well as radiated power. This is attributed to the elimination of ELMs that occurs with large lithium deposition; without the corresponding impurity flushing, the ELM-free regime is commonly observed to be transient with strong particle accumulation. Due to this difficulty in achieving stationary conditions with lithium coatings alone, a cryo-pumping system is being designed for NSTX-U to provide active particle exhaust. The expectation is that this would be used either without lithium, in which case ELMy scenarios can be expected as typical in boronized NSTX scenartios, or with a reduced and optimized lithium deposition amount chosen so that (ideally small and rapid) ELMs remain. This should avoid the impurity accumulation problems of the ELM-free H-mode, and would be more similar to the ELMy H-modes in conventional aspect ratio tokamaks where cryo-pumps are a proven technology for achieving density control.

In addition to facilitating 'particle control' in the sense of avoiding a density that increases throughout the discharge, the cryo-pump will be a critical piece of active control using feedback to maintain the density at desired values. This will be an important capability allowing many physics studies, for example in exploring the role of ν^* in core energy transport. The cryo-pump will provide the particle exhaust needed in conjunction with fueling techniques in order to actively control the plasma density.

b. Physics design

The general layout of the proposed cryo-pumping system is similar to the pump on the lower divertor of DIII-D [95]. As illustrated in Figure 4.2.20, the entrance to the pumping plenum is located on the SOL side of the outer separatrix strike point. The geometry of the plenum entrance (the position of the entrance, along with the height and length of the duct leading to the plenum) has been optimized based on a semi-analytic model for the plenum pressure [95, 96], which was previously developed for the DIII-D pumping system. This model is based on first-flight neutral transport through the divertor plasma (including neutral losses due to ionization) into the plenum entrance, and uses this along with analytic expressions for the pressure in the plenum given the duct geometry and pumping speed. These expressions have been extended as part of the NSTX-U cryo-pump design effort to account for finite duct length at the plenum entrance [97] and the analytic duct conductances as well as plenum pressures has been verified by comparison to calculations using the neutral transport code EIRENE [98].

The analytic pumping model has been used in conjunction with projections of the divertor plasma parameters in order to optimize the height h_{ent} and length g_{ent} of the duct leading into the pumping plenum. Further, an optimization has also been performed to determine the major radius at which the plenum entrance should be placed. This was accomplished using realistic NSTX-U equilibria generated with ISOLVER. Eight equilibria were used, four standard and four snowflake divertors, with the outer strike point position varied from $R_{OSP} \sim 0.5$ to $R_{OSP} \sim 0.7$ m in each configuration. To project the divertor heat flux profile, an exponential profile was assumed with a falloff length given by recent NSTX experiments that measured the SOL heat flux
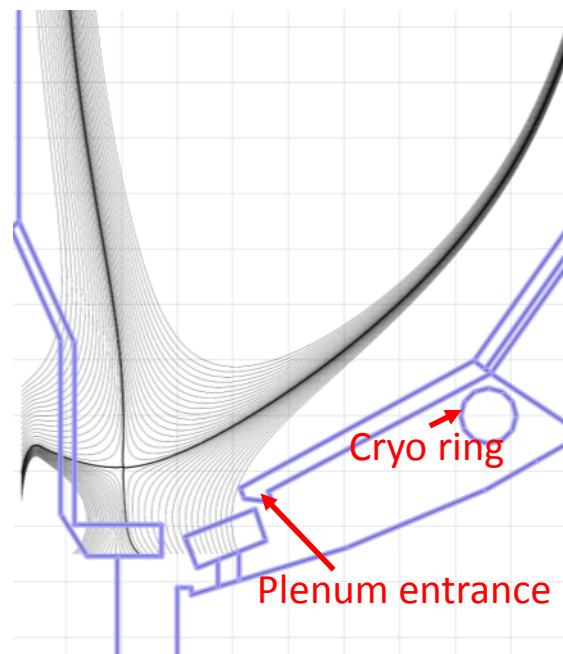

Figure 4.2.20: Layout of the pumping system

width under a variety of conditions.

To assess the effectiveness of the pump, the accessible Greenwald fraction range with the cryo-pump has been estimated. This was accomplished by scanning the divertor T_e in the analytic pumping model and calculating the plenum pressure at each value, then for the T_e at which the pumped flux equals the beam input a two-point model [99] (calibrated to OEDGE modeling and NSTX experiments) was used to estimate the midplane separatrix density. The Greenwald fraction f_G was then calculated assuming the line-averaged density is three time higher than that at the separatrix (based on typical values from NSTX). The resulting f_G is shown in Figure 4.2.21 as a function of separatrix strike point position (which is varies across the set of various equilibria studied) and plasma current (which affects both n_G and λ_q). For the standard divertor configuration (panel a), the achievable f_G is relatively insensitive to plasma current, while the plasma can be pumped down to lower densities if the strike point is moved closer to the plenum entrance (this is similar to the DIII-D experience[96]).

These calculations indicate that the pump should be capable of reducing the plasma density to quite low values, down to $f_G<0.4$ if R_{OSP} is located very near the pump. However, high R_{OSP} configuration have reduced flux expansion, and so at high plasma current (where the SOL is narrowest) it will not likely be possible to move the strike point very near the pump without exceeding the heat flux limit of ~10 MW/m^2 in the standard divertor configuration (the shaded region of the figure shows the region where this limit is exceeded). The snowflake divertor has a significant advantage in this respect, in that the higher flux expansion allows the strike point to be moved closer to the pump without exceeding heat flux limits, so that it should allow operation at higher I_p with good pumping. Further, the snowflake also shows stronger pumping even with the strike point far from the plenum entrance: for $R_{OSP}=0.5$m, the snowflake can be pumped down to $f_G\sim0.6$ compared to $f_G\sim0.8$ in
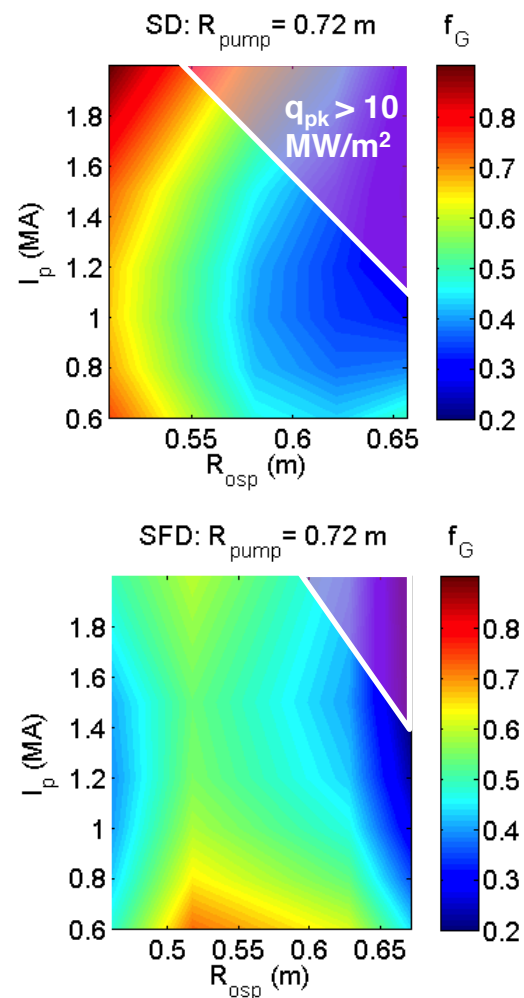

Figure 4.2.21: Estimated Greenwald fraction assuming only neutral beam particle input and cryo-pumping in a) standard and b) snowflake configurations

the standard configuration. While somewhat counterintuitive, the improved pumping in the snowflake is due to the higher flux expansion: with pumping performed in the far SOL as is done here, increasing the flux expansion increases the plasma flux near the pump, which is conducive to higher plenum pressures.

The pumping optimization approach used here is based on a first-flight neutral model, which is expected to be adequate in attached regimes, but to break down in detached divertor cases where charge exchange collisions and diffusive neutral transport are strong. Recently, the analytic model has been checked by comparison to 2D plasma-neutrals modeling with the SOLPS code [REF], which has a much more rigorous neutral transport model that is appropriate in radiative/detached divertor regimes. These calculations showed that in the attached regime (T_e^{div} $> \sim 2eV$), the semi-analytic model is sufficient to predict the plenum pressure (for given plasma parameters). In detached regimes ($T_e^{div} > 2$ eV), the semi-analytic model under-predicts the pressure compared to SOLPS calculations by a factor of 2-3 [97]. These calculations confirm the expectations (based on DIII-D experience) that the analytic model predicts lower pressures than are achieved in detached regimes. Therefore, the use of the semi-analytic model in performing the pumping optimization is conservative, and it can be expected that in detached divertor scenarios the pumping will be even stronger than predicted using these simple estimates.

4.2.3.2. Sustainability of pumping with lithium

Lithium evaporation has been shown to reduce the density ramp rate in the subsequent discharge [7] but substantial amounts of lithium lead to ELM-free operation, with temporally rising electron density and impurity accumulation [100, 101, 102]. The ion inventory can be maintained at a constant or slightly declining level.

Interpretive analysis of discharges with variable lithium conditioning, and hence variable ELM frequency, was done with the SOLPS code to determine if the divertor pumping capacity from lithium was changing with time [8]. It was found that the divertor recycling coefficient R decreased with increasing lithium pre-discharge lithium deposition to a minimum value of R $\sim$ 0.85-0.9, and that this low recycling was maintained for the duration of $\sim$ one sec long discharges [103]. Indeed the divertor recycling as represented by D_α baseline level in those discharges was flat or declining with time. In other words, the time constant for saturating the applied lithium with deuterium bombardment was well over one second.

This conclusion was also corroborated by observations following a large evaporation (50-60 g) of lithium into NSTX; following that evaporation, approximately 100 H-mode discharges were achieved with no additional wall conditioning between discharges (although the discharge reproducibility was not nearly as good as when smaller amounts of lithium were evaporated

between discharges). A similar large evaporation was accomplished on the EAST device [104] in which scientists from NSTX participated. In that study, an e-folding time for evolution of the divertor recycling was ~ 20 sec. These observations provide confidence that lithium wall conditioning would last for the design 5-10 sec pulse length in NSTX-U, but assessment of the duration must be done on NSTX-U, and compared with liquid lithium PFC results.

4.2.3.3. Local recycling, impurity generation and transport studies

An understanding of lithium effects on ion pumping, SOL transport and impurity erosion is emerging from the analysis of spectroscopic data from NSTX experiments [94]. On NSTX-U, this research will be expanded into two main PSI aspects: density and impurity control with lithium and boron coated graphite and high-Z PFCs; it includes the studies of recycling, material erosion and SOL impurity transport.

The methodologies previously applied on NSTX for recycling and impurity influx measurements will be further improved on NSTX-U. The main diagnostics to be used are a new Material Analysis Particle Probe (MAPP) [160], divertor Langmuir probes, and spectroscopy. In particular, (1) ultraviolet and visible spectroscopic measurements of hydrogenic neutrals and neutral or ionized impurity atoms will be used for quantitative influx and source measurements using the S/XB atomic factor method; multi-channel spectrometers or cameras with narrow-bandpass interference filters will be used for these measurements. (2) Impurity emission profiles in combination with local plasma temperature and densities will be used for impurity radial and parallel transport studies aided by interpretive modeling; again, cameras and multi-channel spectrometers will be used for the measurements. (3) Extreme ultraviolet impurity emission in the core plasmas, also in combination with local plasma temperature and densities, will be used for impurity transport and accumulation studies; extreme ultraviolet spectrometers are planned for these measurements.

Because the ion fluxes vary by orders of magnitude from the strike point region to the outer wall, different parts of the wall saturate with deuterium at different times. Estimates of local ion recycling coefficients will be inferred from ratios of the recycled flux (inferred from deuterium Balmer line intensity) to the incident ion flux (inferred from Langmuir probe I_{sat}) with proper inclusion of calibration, atomic and geometry factors. Short (~10 ms) intense deuterium pulse injections from the supersonic gas injector (SGI) will be used to characterize pumping by divertor lithium coatings by measuring the divertor density and D_{α} pump-out times. These experiments will enable characterization both the baseline (lower divertor) or increased area (lower and upper divertor) lithium pumping rates and lifetimes.

In the area of impurity production, the main questions that are to be addressed are (i) accurate accounting of impurity sources for transport studies; (ii) Gross and net erosion fluxes as function

of lithium amount, coverage, and longevity. In the initial years, experiments will be dedicated to lithium and carbon measurements, and as high-Z PFCs are introduced, studies will focus on high-Z erosion and influx measurements. In the area of carbon sources, divertor and midplane C I, C II, CIII, C IV and CD emission profiles will be measured and compared with edge fluid, turbulence and neoclassical edge impurity transport model predictions. The presence of lithium can affect SOL and divertor plasma conditions, change turbulence characteristics, and change parallel forces (e.g., the ion-impurity viscous force and the ion temperature gradient force) that act on divertor impurity ions and regulate divertor retention. This is a critical question for the lithium coating applications, as high Z_{eff} due to carbon was previously observed in NSTX lithium H-mode discharges. In the area of lithium sources, Li I and Li II emission spatial distributions will be measured. Lithium coating lifetime and source strength are dependent on several factors: (1) Lithium erosion process differs from other species in that lithium, being an alkali element, is sputtered as ions (33 %) and neutrals (66 %); (2) because of a low ionization potential and short mean free ionization path, a large fraction of sputtered lithium atoms is re-deposited; (3) because of a low melting temperature (180 C) lithium can melt in the strike point region; (4) lithium erosion rate increases with temperature. In NSTX experiments, the low-level divertor lithium source partially explained very low lithium concentrations in the core plasmas. In the area of high-Z erosion and transport, studies will be initially focused on the basic characterization of high-Z sputtering and transport to the core as a function of boron and lithium coatings, ion and impurity sputtering fluxes, seeded divertor operation, and main plasma heating (e.g., NBI vs HHFW). As the high-Z coverage area is increased, research will be extended to characterize two- and three dimensional erosion distributions (that will also include divertor vs main wall), as well as gross and net erosion fluxes. The ultimate goal of these studies is to understand the PSI with high-Z lithium coated PFCs under seeded or high-flux expansion divertor operations.

4.2.3.4. **Summary of Research Plans by Year**
Year 1 (2014)
- Complete cryo-pump physics design: a) Better establish how much headroom the system gives for pumping beyond the neutral beam input, on which the present design is based; b) Continue calculations in high density partly detached regime with additional gas input with fluid codes

Years 2-3
- Perform cryo-pump engineering design and install pump, based on the finalized physics design from projected divertor plasma parameters
- Validate cryo-pump physics design calculations which assumed SOL profiles of divertor parameters from NSTX projections, by comparing with initial measurements in NSTX-U
- Assess ability of lithium conditioning to provide density and impurity control for high power, long pulse NSTX-U discharges, using a combination of the downward

evaporators in the first year of operation, combined with upward-facing evaporator(s) in the second year of operation

- Assess lithium coating lifetimes and interaction with ion fluxes in divertor strike point, near-SOL and far-SOL regions with spectroscopy
- Extend local hydrogenic recycling and particle balance measurements to the upper and lower divertor areas, and main wall, including comparisons of boronized and lithium-coated graphite plasma-facing components

Years 4-5

- Characterize performance of pump to compare with design calculations, and also with perform with lithium conditioning
- Assess pump performance with metallic PFCs, as those are introduced into NSTX-U
- Develop scenarios use the cryo-pump for deuterium control while maintaining ELMs for impurity flushing, similar to conventional tokamak operating scenarios; this will inform the use of the cryo-pump in density control schemes described in Chapter 9

4.3 Summary of Theory and Simulation capabilities

4.3.1. XGC Total-f Gyrokinetic Particle Code

XGC1 is a nonlinear gyrokinetic particle-in-cell code for kinetic ions, electrons, and neutrals in realistic diverted tokamak magnetic geometry. Coulomb collisions conserve particle, momentum, and energy, with the option of linearized or fully nonlinear operators. The main difference between XGC1 and the other US gyrokinetic codes is that XGC1 is a total-f code while the others are delta-f codes. In a total-f code, the background plasma profiles, electric field, and rotation evolve self-consistently with external heat source, heat sink, turbulence and transport; while in a delta-f code, the turbulence and transport is evaluated from an assumed fixed plasma background. Neoclassical physics is automatically included in a total-f gyrokinetic code while it is not in a delta-f gyrokinetic code. As a result, the plasma and transport profiles settle to a self-organized state in XGC1, similarly to experimental situation, consistently with externally applied heat source and edge loss. On the other hand, in a delta-f code, transport fluxes vary sensitively to the assumed plasma profile. XGC1 can also be operated in delta-f mode for diagnostics purposes. Spatial simulation domain of XGC1 is usually the whole tokamak volume: from the magnetic axis to the material wall, across the magnetic separatrix surface. In order to reduce the computing time requirement, physics research emphasis is given to the pedestal/SOC region by allowing a more refined grid in that region. An inner radial boundary can be specified in an edge only simulation. However, it is found that the artificial boundary condition distorts the edge turbulence solution. Most of the past study by XGC1 has been performed for the study of nonlinear ITG turbulence and neoclassical physics with adiabatic electrons. Recent studies

include the wall-recycled Monte Carlo neutral particles with charge exchange and ionization physics, and non-adiabatic kinetic electrons in electrostatic turbulence mode. Transition physics from ITG to TEM has been cross-verified with other codes in delta-f simulation mode. XGC1 is under verification for electromagnetic turbulence. Impurity particles with wall sputtering coefficient are being added. Interaction of 3D RMP physics with plasma turbulence will be studied in the near future. All of these processes and effects: turbulence, neoclassical, neutral, impurity, and wall interaction physics, are simulated self-consistently.

4.3.2. XGC0 total-f Axisymmetric Particle Code

XGC0 is the axisymmetric version of XGC1, which ignores turbulence. Instead, turbulent transport is incorporated in the neoclassical Lagrangian particle motion as a radial random walk process. Since XGC0 does not have toroidal grids and uses a much smaller number of poloidal grid points, simulation speed is about 100X faster. Simulations of kinetic plasma profile evolution, pedestal buildup and divertor heat load accumulation are performed usually within a day on a local cluster or on a moderate size HPC, depending upon the physics. For this reason, XGC0 is more popular to experimental users than XGC1 is. Currently, XGC0 contains kinetic ions, kinetic electrons, Monte Carlo neutral particles with ionization and charge exchange cross-sections, multispecies impurities with radiative power loss, logical wall-sheath, heat source, and momentum source. A particle, momentum, and energy conserving Coulomb collision operator is used in linearized and fully nonlinear modes. 3D RMP penetration into plasma is studied with the added perturbed magnetic field solver to the existing electrostatic solver. The gyrokinetic neoclassical effect and the poloidal electrostic potential variation solver are under addition in XGC0. In the future, XGC0 and XGC1 will be combined in subgrid time-integration technique for experimental time-scale simulation of gyrokinetic turbulence, neoclassical and other important physics. XGC0 is coupled to M3D code for pedestal-ELM cycle study.

4.3.3. DEGAS - described in Macrostability Chapter 2

4.3.4 BOUT++

A three-dimensional realistic tokamak geometry edge electromagnetic turbulence and MHD code that solves Braginskii-like fluid equations for ion density, parallel ion and electron velocities, separate electron and ion temperatures, vorticity equation for electrostatic potential, and vector potential $A_\parallel$ equation [147].

4.3.5. The UEDGE code

UEDGE is an edge multi-fluid transport code that simulates plasma, neutral and photon transport in the tokamak SOL and divertor region. The code is based on the solution of the Braginskii-like

fluid equations for ion density, parallel velocity, separate electron and ion temperatures, vorticity equation, neutral density, and neutral parallel velocity [105, 106, 107, 108]. The computational mesh is based on the magnetic equilibrium obtained from MHD equilibrium codes. The plasma transport is classical along the magnetic field with the addition of flux limits for kinetic corrections. The transport across the magnetic field is described by ad-hoc diffusion and convection coefficients. UEDGE also includes the option to model classical cross-magnetic-field drifts associated with E **x** B and gradient-**B**/curvature drifts. Impurity species are treated either in a fixed fraction approximation, or by following the separate charge-state ions. The sputtering of divertor and wall materials as an impurity source is included via physical and chemical yield functions. For neutral species, a fluid model is used, with particle and energy flux limiters determined by thermal streaming values based on a comparison with more detailed Monte-Carlo neutral simulations. Direct coupling to a Monte-Carlo neutral transport code DEGAS 2 is also implemented. The basic UEDGE models have been used extensively to model edge plasma characteristics in a number of existing tokamaks, e.g. DIII-D [109], NSTX [110,111], Alcator C-Mod [112] and JT60-U [113] as well as ITER [114] and some ARIES designs [110].
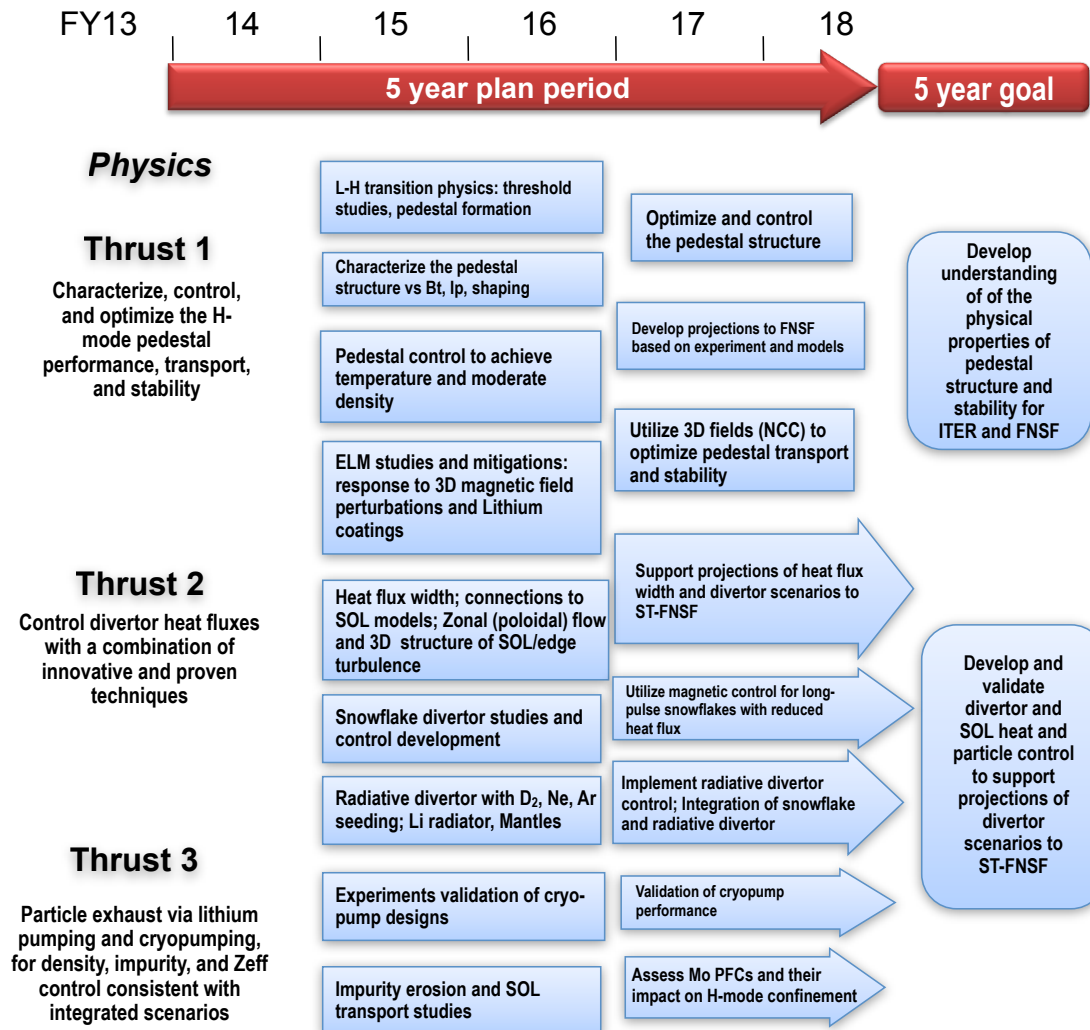
4.3.6. The SOLT code

The Scrape-Off-Layer Turbulence (SOLT) code [115] is a fluid code that models turbulence in a two-dimensional plane perpendicular to the magnetic field B at the outboard midplane of the torus. SOLT implements classical parallel physics using closure relations [116] for the midplane parallel current and parallel fluxes of particles and energy for collisional regimes ranging from sheath-connected to conduction limited. The SOLT code can describe arbitrarily strong nonlinear plasma dynamics ($\delta n/n \sim 1$), including blob-filaments [116, 118], and the physics model supports interchange-type curvature-driven modes, sheath and Kelvin-Helmholtz (KH) instabilities, and drift waves. Past versions have assumed cold ions; current development work [119] is implementing finite ion pressure including the relevant ion gyroviscous terms, and additionally removes the commonly used but hard-to-justify Boussinesq approximation. For comparison with experimental gas puff imaging data, SOLT employs a synthetic GPI diagnostic to simulate both He and D gas puffs. Recent applications of SOLT have included the study of zonal flow oscillations [120], the effect of parallel currents on turbulence [121], SOL heat flux widths [117, 122, 123], a SOLT quasi-coherent mode [121], and the impact of edge topology and profiles on the generation of flows [124].

4.3.7. The SOLPS suite of codes

The SOLPS suite of codes solve a set of 2-D equations for the coupled plasma and neutral transport[125]. The plasma is treated with a 2-D fluid approximation using the B2.5 code [126] with transport parallel to the magnetic field governed by classical Braginskii-type equations

(with corrections for kinetic effects) and cross-field transport given by user-specified "anomalous" transport coefficients. Neutral transport is calculated by the EIRENE Monte Carlo code[98], a the code has the ability to treat multiple impurity species.

2014-18 Boundary Physics Research Timeline

Physics

Thrust 1

Characterize, control, and optimize the H-mode pedestal performance, transport, and stability

Thrust 2

Control divertor heat fluxes with a combination of innovative and proven techniques

Thrust 3

Particle exhaust via lithium pumping and cryopumping, for density, impurity, and Zeff control consistent with integrated scenarios

2014-18 Boundary Physics Research Timeline

FY13   14   15   16   17   18

5 year plan period

1 year outage between FY2016 and FY2017

Tools

Diagnostics

- Upgraded MPTS
- 2D BES
- Center stack IR camera
- Divertor Thomson Scattering system (*incremental*)
- Divertor Langmuir probes, bolometry
- Divertor ion energy or temperature (fast thermocouple), and SOL current sensors
- Upper divertor spectroscopic sightlines & IR cameras; Divertor spectroscopy (VUV, visible)
- Upgraded edge and divertor bolometry
- Edge profile reflectometry
- Reflectometry
- Real-time density measurements: Interferometry and MPTS

Facility

- Lithium granule injection; improved Liters
- Partial NCC
- Edge gas injection and SGI with PCS feedback control
- High-Z tile row on cryo-baffle and on top
- Divertor gas injectors
- Upward LiTER
- Cryo-pumping & associated diagnostics
- Improved divertor tile alignment
- EHO antenna (*incremental*)
- High-Z tile row

Plasma Control

- Control of divertor coils for X- and strike-point positions
- control scenarios using both strike-point and cryopump
- Implement and advance snowflake divertor configuration control
- Gas injection feedback control; PCS control of divertor gas injection
- Radiative divertor control

4.54

References

[1] "Priorities, Gaps, and Opportunities: Towards a Long Range Strategic Plan for Magnetic Fusion Energy, FESAC Greenwald Panel Report, 2007.

[2] "Research Needs (ReNeW) for Magnetic Fusion Energy Science", June 9-13, 2009.

[3] "Report of the FESAC Subcommittee on the Priorities of the Magnetic Fusion Energy Science Program", Rosner Panel, 2013.

[4] Eich, T., *et al.,* Physical Review Letters 107 (2011) 215001.

[5] Goldston, R., Nuclear Fusion 52 (2012) 013009.

[6] Makowski, M. A., *et al.*, Physics of Plasmas 19 (2012) 056122.

[7] Maingi, R., *et al.*, Physical Review Letters 103 (2009) 075001.

[8] Canik, J. M., *et al.*, Physics of Plasmas 18 (2011) 056118.

[9] Boyle, D. P., *et al.*, Plasma Physics and Controlled Fusion 53 (2011) 105011.

[10] Maingi, R., *et al.*, Nuclear Fusion 50 (2010) 064010.

[11] Kaye, S., *et al.*, Nuclear Fusion 51 (2011) 113019.

[12] Battaglia, D., *et al.*, Submitted to Nuclear Fusion, 2013.

[13] Chang, C., *et al.*, Phys. of Plasmas 11 (2004) 2469.

[14] Zweben, S., *et al.*, Physics of Plasmas 17 (2010) 102502.

[15] Maqueda, R., *et al.*, Nuclear Fusion 50 (2010) 075002.

[16] Snyder, P. B., *et al.*, Phys. Plasmas 16 (2009) 056118.

[17] Callen, J. D., Phys. of Plasmas 12 (2005) 092512.

[18] Dickinson, D., *et al.*, Phys. Rev. Lett. 108 (2012) 135002.

[19] Callen, J. D., Canik, J. M., and Smith, S. P., Phys. Rev. Lett. 108 (2012) 245003.

[20] Diallo, A., et al., Nuclear Fusion 51 (2011) 103031.

[21] Diallo, A., *et al.*, Physics of Plasmas 20 (2013) 012505.

[22] Snyder, P. B., *et al.*, Phys. of Plasmas 9 (2002) 2037.

[23] Diallo, A., *et al.*, Submitted to Nucl. Fusion, 2013.

[24] Kaw. P. *et al.*, Submitted to Nucl. Fusion, 2013.

[25] Snyder, P., *et al.*, Nuclear Fusion 51 (2011) 103016.

[26] Snyder, P. B., *et al.*, Plasma Phys. Control. Fusion (46) A131.

[27] Sontag, A., *et al.*, Nuclear Fusion 51 (2011) 103022.

[28] Smith, D., *et al.*, Accepted to Phys. Plasma, 2013.

[29] Canik, J.M., *et al.*, Submitted to Nucl. Fusion 2013.

[30] Chen, Y. and Parker, S., J. Comput. Phys. 220 (2007) 839.

[31] Maingi, R., *et al.*, Nucl. Fusion 45 (2005) 1066.

[32] Maingi, R., *et al.,* Nuclear Fusion 51 (2011) 063036.

[33] Maingi, R., *et al.*, Nucl. Fusion 45 (2005) 264.

[34] Connor, J. W., *et al.*, Phys. of Plasmas 5 (1998) 2687.

[35] Ahn, J.-W., *et al.*, Review of Scientific Instruments 81 (2010) 023501.

[36] Evans, T., *et al.*, Phys. Rev. Lett. 92 (2004) 235001.

[37] Canik, J., *et al.*, Nuclear Fusion 50 (2010) 034012.

[38] Canik, J., *et al.*, Nuclear Fusion 52 (2012) 054004.

[39] Evans, T., *et al.*, Nuclear Fusion 48 (2008) 024002.

[40] Unterberg, E., *et al.*, J. Nucl. Mat. 390 (2009) 486.

[41] Fenstermacher, M., *et al.*, Nuclear Fusion 48 (2008) 122001.
[42] Baylor, L., *et al.*, Submitted to Nucl. Fusion 2013.
[43] Mansfield, D., *et al.*, Submitted to Nucl. Fusion 2013.
[44] Maingi, R., *et al.*, Nuclear Fusion 52 (2012) 083001.
[45] Greenfield, C., *et al.*, Phys. Rev. Lett. 86 (2001) 4544.
[46] Suttrop, W., *et al.*, Plasma Physics and Controlled Fusion 46 (2004) A151.
[47] Burrell, K. H., *et al.*, Physics of Plasmas 12 (2005) 056121.
[48] Park, J.-K., *et al.*, To be published in Nucl. Fusion 2013.
[49] Gerhardt, S., *et al.*, Nuclear Fusion 50 (2010) 064015.
[50] Takahashi, H., *et al.*, Nuclear Fusion 44 (2004) 1075.
[51] Takahashi, H., *et al.*, Phys. Rev. Lett. 100 (2008) 205001.
[52] Evans, T., *et al.*, J. Nucl. Mat. 390 (2009) 789.
[53] Maingi, R., *et al.*, Phys. Rev. Lett. 105 (2010) 135004.
[54] Maingi, R., *et al.*, J. Nucl. Mat. 390 (2009) 440.
[55] Whyte, D. *et al.*, Nucl. Fusion 50 (2010) 105005.
[56] Maingi, R., *et al.*, NSTX Report on FES Joint Research Milestone 2010 and PPPL report 4700, 2011.
[57] Gray, T., *et al.*, J. Nucl. Mater. 415 (2011) S360.
[58] Goldston, R., *et al.*, To be published in J. Nucl. Mat. 2013, 2013.
[59] Belli, E. A. and Candy, J., Plasma Physics and Controlled Fusion 54 (2012) 015015.
[60] Sugiyama, L. E. and Strauss, H. R., Physics of Plasmas 17 (2010) 062505.
[61] Green, D., *et al.*, Phys. Rev. Lett. 107 (2011) 145001.
[62] Angus, J., *et al.*, Phys. Rev. Lett. 108 (2012) 215002.
[63] Mosetto, A., *et al.*, Phys. of Plasmas 19 (2012) 112013.
[64] Baver, D., *et al.*, Computer Physics Comm. 182 (2011) 1610.
[65] Angus, J., *et al.*, Contrib. Plasma Phys. 52 (2012) 348.
[66] Ku, S., Chang, C., and Diamond, P., Nuclear Fusion 49 (2009) 115021.
[67] Myra, J. *et al.*, Phys. Plasmas 18 (2011).
[68] Kubota, S., *et al.*, Rev. Sci. Instrum. 81 (2010) 10D917.
[69] Cao, B., *et al.*, Plasma Phys. Control. Fusion 54 (2012) 112001.
[70] Jaworski, M., *et al.*, Fusion Eng. Des. 87 (2012) 1711.
[71] Soukhanovskii, V. A., *et al.*, J. Nucl. Mater. 337-339 (2005) 475.
[72] Soukhanovskii, V., *et al.*, Phys. Plasmas 16 (2009) 022501.
[73] Soukhanovskii, V., *et al.*, Nucl. Fusion 49 (2009) 095025.
[74] Loarte, A., *et al.*, Nucl. Fusion 47 (2007) S203.
[75] Stangeby, P. C., The plasma boundary of Magnetic Fusion Devices, IoP, Bristol, 2000.
[76] Goswami, R., *et al.*, Physics of Plasmas 8 (2001) 857.
[77] Rognlien, *et al.*, Contrib. Plasma Phys. 44 (2004) 188.
[78] ITER physics expert group on divertor, on divertor modelling, database, and editors, I. P. B., Nucl. Fusion 39 (1999) 2391.
[79] Ryutov, D., Phys. Plasmas 14 (2007) 64502.
[80] Kotschenreuther, M., *et al.*, Phys. Plasmas 14 (2007) 72502.
[81] Piras, F., *et al.*, Plasma Phys. Control. Fusion 51 (2009) 055009.
[82] Piras, F., *et al.*, Plasma Phys. Control. Fusion 52 (2010) 124010.
[83] Piras, F., *et al.*, Phys. Rev. Lett. 105 (2010) 155003.

[84] Soukhanovskii, V., *et al.*, Nucl. Fusion 51 (2011) 012001.
[85] Soukhanovskii, V., *et al.*, J. Nucl. Mater. 415 (2011) S365.
[86] Soukhanovskii, *et al.*, Phys. Plasmas 19 (2012) 082504.
[87] Rognlien, T. D., *et al.*, J. Nucl. Mater. 196-198 (1992) 347.
[88] Ryutov, D. and Umansky, M., Phys. Plasmas 17 (2010) 014501.
[89] Ryutov, D. D., *et al.*, Plasma Physics and Controlled Fusion 54 (2012).
[90] Valanju, P., *et al.*, Phys. Plasmas 16 (2009) 056110.
[91] Mandrekas, J. and Stacey, W.M., J., Nucl. Fusion 35 (1995) 843.
[92] Yamada, I., *et al.*, Plasma Fusion Res. 5 (2010) S2033.
[93] Matthews, G., *et al.*, J. Nucl. Mater. 241-243 (1997) 450.
[94] Soukhanovskii, V., *et al.*, Rev. Sci. Instrum. 83 (2012) 10; Scotti F. *et al.*, Rev. Sci. Instrum. 83, 10E532 (2012)
[95] Maingi, R., *et al.*, Nucl. Fusion 39 (1999) 1187.
[96] Maingi, R., *et al.*, Nuc. Fusion 44 (2004) 909.
[97] Canik, J., *et al.*, APS-DPP 2012, 2012.
[98] Reiter, D., *et al.*, Fusion Sci. Tech. 47 (2005) 172.
[99] Stangeby, P., The Plasma Boundary of Magnetic Fusion Devices, Bristol: Institute of Physics Publishing, 2000.
[100] Kugel, H., *et al.*, Journal of Nuclear Materials 390-391 (2009) 1000.
[101] Mansfield, D., *et al.*, Journal of Nuclear Materials 390-391 (2009) 764.
[102] Bell, M. G., *et al.*, Plasma Physics and Controlled Fusion 51 (2009) 124054.
[103] Boyle, D., Submitted PSI 2013.
[104] Guo, D.*, et al.*, Submitted to Science, 2013.
[105] Rognlien T.D. and Rensink M.E., Fusion Eng. Design 60 (2002) 497.
[106] Rognlien T.D., Rensink M.E. and Smith G.R. 2000, User Manual for the UEDGE edge-plasma transport code, Lawrence Livermore National Lab Report UCRL-ID-137121.
[107] Rognlien T.D., *et al.*, J. Nucl. Mater. 363–365 (2007) 658.
[108] Braginskii S.I. 1965 Transport processes in a plasma Reviews of Plasma Physics vol 1 ed M.A. Leontovich (New York: Consultants Bureau) p 205.
[109] Porter G.D., *et al.*, Fusion Sci. Technol. 48 (2005) 1127.
[110] Rensink, M.E., *et al.,* J. Nucl. Mater. 290–293 (2001) 706.
[111] Smirnov R.D. *et al.*, Contrib. Plasma Phys. 50 (2010) 299.
[112] Pigarov A.Yu., et al., J. Nucl. Mater. 363–365 (2007) 643.
[113] Takenaga H., *et al.,* Nucl. Fusion 45 (2010) 1618
[114] Rognlien T.D., *et al.,* J. Nucl. Mater. 363–365 (2007) 658
[115] D. A. Russell, J. R. Myra and D. A. D'Ippolito Phys. Plasmas 16, 122304 (2009).
[116] Krasheninnikov S.I., D. A. D'Ippolito and J. R. Myra, J. Plasma Phys. 74, 679 (2008).
[117] Myra, J.R., *et al*., Phys. Plasmas 18, 012305 (2011).
[118] D'Ippolito, D.A., J.R. Myra and S. J. Zweben, Phys. Plasmas 18, 060501 (2011).
[119] Russell D.A., D.A. D'Ippolito and J.R. Myra, 54th APS/DPP Meeting, Providence, Rhode Island, October 29 - November 2, 2012, paper BP8-159.
[120] Sechrest Y., *et al*., Phys. Plasmas 18, 012502 (2011).

[121] D'Ippolito D.A., et al., Phys. Plasmas 19, 102301 (2012).

[122] Russell, D.A., *et al.*, Phys. Plasmas 19, 082311 (2012).

[123] Myra, D.A., *et al.*, Plasma Physics and Controlled Fusion 54, 055008 (2012).

[124] Myra J.R., *et al.*, 24th IAEA Fusion Energy Conference, San Diego, USA, October 8 - 13, 2012, paper IAEA-CN-197/TH/P4-23

[125] Schneider R., *et al.,* Contrib. Plasma Phys. 46, 3 (2006).

[126] Braams B.J., Contrib. Plasma Phys. 36, 276 (1996).

[127] Hirshman S.P., *et al.*, Comput. Phys. Commun. 43 (1986) 143.

[128] Sanchez R., *et al.,* Comput. Phys. Commun. 135 (2001) 82.

[129] Gray T.K. *et al.*, J. Nucl. Mater. 415 (2011) S360; V. Soukhanovskii *et al.*, 36th EPS 2009 Proceedings, paper 2.178.

[130] Petrie T. W. *et al.*, Nucl. Fusion 37 (1997) 321, and references therein.

[131] Gray T.K., *et al.* J. Nucl. Mater. 2013 at press.

[132] Martin Y., *et al.*, J. Conf. Phys. Series 123 (2008) 012033.

[133] Bush C.E., *et al.*, Phys. Plasmas 10 (2003) 1755.

[134] Loarte A. *et al.*, Phys. Scripta T128 (2007) 222.

[135] Gan K.F. *et al.*, PPCF 2013 submitted.

[136] Ahn J.W *et al.*, J. Nucl. Mater. 2013 at press.

[137] Yan Z. *et al.*, Phys. Rev. Lett., 107 (2011) 055004.

[138] Guttenfelder W. *et al.*, Nucl. Fusion (2013) submitted.

[139] Snyder P.B., *et al.* Nucl Fusion 47 (2007) 961.

[140] Nazikian R., Private Comm, 2013.

[141] Huysmans G.T.A. *et al.*, PPCF 51 (2009) 124012.

[142] Dudson B. *et al.,* Computer Physics Communications 180 (2009), 1467.

[143] Kirk A *et al* 2009 Plasma Phys. Control. Fusion 51 065016.

[144] Koh S. *et al.*, Phys. Plasmas 19 (2012) 072505.

[145] Sauter O. *et al.*, Phys. Plasmas 6 (1999) 2834.

[146] Greenwald M. *et al.*, Nucl. Fusion 28 (1988) 2199.

[147] Conway G.D. *et al.,* Phys. Rev. Lett. 106 (2011) 065001; Schmitz L. *et al.*, Phys. Rev. Lett. 108 (2011) 155002.

[148] Osborne T.H. *et al.*, Plasma Phys. Cont. Fusion 49 (1998) 845.

[149] Zohm H. *et al.*, Plasma. Phys. Cont. Fusion 38 (1996) 845.

[150] Wilson H.R. *et al.*, Phys. Plasmas 9 (2002) 1277.

[151] Wilson H.R. *et al.*, Plasma. Phys. Cont. Fusion 48 (2006) A71.

[152] Oyama N. *et al.*, *et al.*, Plasma. Phys. Cont. Fusion 48 (2006) A171.

[153] Chang C.S. *et al.*, submitted to Nucl. Fusion 2013.

[154] Ferraro N.M. *et al.*, Phys. Plasmas 17 (2010) 102508.

[155] Kotschenreuther M. *et al.*, Comp. Phys. Comm. 88 (1995) 128.

[156] Jenko F. *et al.*, Phys. Plasmas 7 (2000) 1904.

[157] Eich T. *et al.*, Nucl. Fusion 2013 submitted.

[158] McClean A.G. *et al.*, Rev. Sci. Instrum. 83, 053706 (2012).
[159] Valanju P. *et al.*, Phys. Plasmas 16 (2009) 056110.
[160] Taylor C.N. *et al.*, Rev. Sci. Instrum. 83 (2012) 10D703